



Magnetic buoyancy in simulated galactic discs with a realistic circumgalactic medium

U. P. Steinwandel,^{1,2,3*} M. C. Beck,³ A. Arth,^{1,4} K. Dolag,^{1,2} B. P. Moster^{1,2} and P. Nielaba³

¹Universitäts-Sternwarte München, Scheinerstr 1, 81679 München

²Max Planck Institute for Astrophysics, Karl-Schwarzschild-Str 1, 85741 Garching, Germany

³Department of Physics, University of Konstanz, Universitätsstr 10, 78457 Konstanz, Germany

⁴Max Planck Institute for Extraterrestrial Physics, Giessenbachstr 1, 85748 Garching, Germany

Accepted 2018 November 8. Received 2018 October 18; in original form 2018 August 29

ABSTRACT

We present simulations of isolated disc galaxies in a realistic environment performed with the Tree-SPMHD-Code GADGET-3. Our simulations include a spherical circumgalactic medium (CGM) surrounding the galactic disc, motivated by observations and the results of cosmological simulations. We present three galactic models with different halo masses between 10^{10} and 10^{12} M_\odot , and for each we use two different approaches to seed the magnetic field as well as a control simulation without a magnetic field. We find that the amplification of the magnetic field in the centre of the disc leads to a biconical magnetic outflow of gas that magnetizes the CGM. This biconical magnetic outflow reduces the star formation rate (SFR) of the galaxy by roughly 40 per cent compared to the simulations without magnetic fields. As the key aspect of our simulations, we find that small-scale turbulent motion of the gas in the disc leads to the amplification of the magnetic field up to tens of μG , as long as the magnetic field strength is low. For stronger magnetic fields, turbulent motion does not lead to significant amplification but is replaced by an $\alpha-\omega$ dynamo. The occurrence of a small-scale turbulent dynamo becomes apparent through the magnetic power spectrum and analysis of the field lines' curvature. In accordance with recent observations, we find an anticorrelation between the spiral structure in the gas density and in the magnetic field due to a diffusion term added to the induction equation.

Key words: methods: numerical – galaxies: evolution – galaxies: formation – galaxies: general – galaxies: magnetic fields.

1 INTRODUCTION

Magnetic fields are a fundamental aspect in astrophysics and cosmology. They are essential for describing many processes in theoretical astrophysics properly. The relevance of magnetic fields ranges from the small scales in star formation and in the interstellar medium (ISM) over galactic scales up to galaxy clusters and the large-scale structure of the Universe. While there is a large amount of observational data on magnetic fields, especially in the area of galaxy formation and evolution (i.e. Hummel 1986; Chyží et al. 2003, 2007; Beck 2007), the situation is different for numerical studies that investigate the behaviour of magnetic fields in detail (Kotarba et al. 2011; Pakmor & Springel 2013; Beck et al. 2016a; Rieder & Teyssier 2016; Pakmor et al. 2017). In the case of galaxies, the magnetic field becomes important for several reasons. It acts as an

additional pressure component, and thus is needed as a correction of the equations of hydrodynamics, resulting in the well-known equations of magnetohydrodynamics. Moreover, the magnetic pressure in galaxies can reach the same order of magnitude as the turbulent pressure of the ISM, and thus it can completely dominate the thermal pressure of the disc. Hence, it should be taken into account in simulations of galaxy formation and evolution. However, this is often not the case and pure hydrodynamical simulations are used to study the formation and evolution of galactic discs. On the other hand, magnetic fields can be very important for star formation and the regularization of cosmic rays and should not be excluded when these processes are taken into account.

Still, the origin of magnetic fields in the Universe is unclear. It is possible to generate magnetic seed fields below 10^{-20} G by either battery processes in the early Universe (e.g. Biermann 1950; Mishustin & Ruzmaikin 1972; Zeldovich, Ruzmaikin & Sokolov 1983) or the phase transitions that appear in the standard model, shortly after the Big Bang (e.g. Hogan 1983; Ruzmaikin, Sokolov &

* E-mail: usteinw@usm.lmu.de

Shukurov 1988a,b; Widrow 2002). Those initial magnetic fields can then be amplified by various dynamo processes, namely the $\alpha-\omega$ dynamo (Ruzmaikin et al. 1979), the cosmic ray driven dynamo (Lesch & Hanasz 2003; Hanasz et al. 2009) or the small-scale turbulent dynamo (Kazantsev 1968; Kraichnan 1968). While the first and the second dynamo process operate on 10^8 yr-scales, the third process has typical time-scales in the Myr-regime (Biermann & Schlüter 1951). The magnetic energy is exponentially amplified on the small scales and random motion regulates it on the largest turbulent scales (Zeldovich et al. 1983; Kulsrud & Anderson 1992; Kulsrud et al. 1997; Malyshkin & Kulsrud 2002; Schekochihin et al. 2002, 2004; Schleicher et al. 2010).

Observationally, there are several methods to measure the magnetic field strengths in galaxies. Brown et al. (2007) investigated the magnetic field of the inner Milky Way using rotation measurements of 148 objects behind the galactic disc. More recent observations from Han et al. (2018) present rotation measurements of 477 pulsars and compared their distribution with extra galactic radio sources showing that the magnetic field of the Milky Way has a bisymmetric structure. Further, magnetic fields of nearby galaxies can be determined using their radio synchrotron emission. In this case, the unpolarized component of the synchrotron emission is important because it is needed to explain galactic dynamics and magnetic-driven outflows (Beck 2007). Radio synchrotron emission is also used to calculate the magnetic field strengths in nearby galaxies that leads to values between 20 and 30 μG in the spiral arms and to 50–100 μG in the galactic centre, as described in Beck (2007) or Beck (2009). Robishaw, Quataert & Heiles (2008) presented measurements of magnetic fields due to Zeeman-splitting emission in OH megamasers of five ultraluminous infrared galaxies leading to magnetic field strengths along the line of sight between 0.5 and 18 mG. Beyond the observations of the magnetic fields in galactic discs, there are also those of their circumgalactic medium (CGM). Carretti et al. (2013) present measurements of magnetized outflows towards the CGM of the Milky Way in two giant lobes located in the north and south of the galactic centre with a magnetic field strength of around 15 μG , known as the ‘Fermi bubbles’.

Simulations of galactic magnetic fields are often done with hydrodynamical grid codes. Wang & Abel (2009) investigated the magnetic field in isolated disc galaxies without star formation using the grid code ENZO (Bryan & Norman 1997; O’Shea et al. 2004; Bryan et al. 2014). Dubois & Teyssier (2010) studied the magnetic field of dwarf galaxies with a closer look on winds driven by stars using the grid code RAMSES (Teyssier 2002). Pakmor & Springel (2013) and Rieder & Teyssier (2016) present studies of magnetic fields for isolated galaxy formation by collapsing a giant gaseous halo in a dark matter potential using the moving mesh code AREPO (Springel 2010) and the grid code RAMSES, respectively. While Pakmor & Springel (2013) investigate general properties of the magnetic field, Rieder & Teyssier (2016) point out the importance of supernova (SN) feedback on the structure of the ISM and its magnetic field. Another detailed study of magnetic fields in isolated discs is presented in Butsky et al. (2017) where they find a small-scale turbulent dynamo of the magnetic field. The same behaviour can be found in Rieder & Teyssier (2017a) for an isolated disc galaxy as well as in Pakmor et al. (2017) and Rieder & Teyssier (2017b) for cosmological zoom-in simulations. The evolution of magnetic fields has been extensively studied with particle-based methods for magnetohydrodynamics as well. Kotarba et al. (2009) investigate the magnetic field in an isolated disc galaxy using the SPH-code VINE (Wetzstein et al. 2009). In Kotarba et al. (2010), VINE is used for studies of the magnetic field in the Antennas galaxies. In

Kotarba et al. (2011), Geng et al. (2012a), and in Geng et al. (2012b), GADGET-3 is used to study the magnetic field in other galaxy mergers. Beck et al. (2016a) is investigating the magnetic field structure of the Milky Way in more detail, by calculating its synchrotron emission. Many of these simulations study the evolution of galaxies in isolation by sampling a dark matter halo, a stellar bulge, and a stellar and gaseous disc to create the initial conditions. The hot CGM is typically neglected to save computational effort and as it is mainly irrelevant for galactic dynamics. However, cosmological simulations show that galaxies are constantly accreting gas from their hot haloes, such that this component is essential to model realistic galactic systems. Moreover, a hot gaseous halo around the Milky Way can now be detected observationally (Miller & Bregman 2013). These observations indicate that the density profile of the CGM can be described with a β -power law (Cavaliere & Fusco-Femiano 1978), which is common in studies of globular clusters (Plummer 1911) and cosmological simulations of galaxy clusters (e.g. Donnert 2014). Consequently, it may be critical to include the hot gaseous component in simulations of isolated galaxies. In SPMHD simulations, the presence of the CGM has a further advantage. In the SPMHD formalism, the magnetic field is a property of the gas particles. Therefore, a carrier for the magnetic field is needed that gives further justification for the presence of the CGM in magnetohydrodynamic simulations. In this work, we present a set of nine high-resolution simulations that include a spherical hot CGM for each galaxy. The paper is structured as follows. We give a short summary of our simulation method in Section 2, where we point out recent improvements of our numerical methods and the physical models that are considered. In Section 3, we present the methods that we use to build our numerical model for an isolated disc galaxy that includes an observationally constrained CGM. We then examine the general properties of each galactic system and investigate the interaction between the galactic disc and the CGM in Section 4. Our conclusions are presented in Section 5.

2 SIMULATION METHOD

The simulations we present in this paper are performed using the Tree-SPMHD-Code GADGET-3, the developers version of the public available GADGET-2 code (Springel 2005). We use a modern implementation of SPH, as presented in Beck et al. (2016b). This SPH formulation includes various improvements such as a higher order SPH-kernel described by Dehnen & Aly (2012), a time-step limiter (Dalla Vecchia & Schaye 2012), time-dependent artificial viscosity, and a new model for time-dependent artificial conduction. Our version of GADGET-3 further includes magnetic fields and magnetic dissipation as presented in Dolag & Stasyszyn (2009). We also include star formation, cooling, SN feedback, and metals following Springel & Hernquist (2003). Further, one of our models for the magnetic field couples the seed rate of the magnetic field directly to the SN rate within the ISM, as presented in Beck et al. (2013). In this section, we summarize the adopted SPH formalism and the physical models in a very compact way.

2.1 Kernel function and density estimate

We use the density–entropy formulation of SPH, i.e. we smooth the density distribution such that

$$\rho_i = \sum_j m_j W_{ij}(x_{ij}, h_i), \quad (1)$$

where h_i is the smoothing length. The sum in equation (1) is calculated over the neighbouring particles. $W_{ij}(x_{ij}, h_i)$ is the smoothing kernel with the property

$$W_{ij}(x_{ij}, h_i) = \frac{1}{h_i^3} w(q). \quad (2)$$

In our simulations, we use the Wendland C4 function for $w(q)$, with 200 neighbouring particles. The function $w(q)$ is given by

$$w(q) = \frac{495}{32\pi} (1 - q)^6 \left(1 + 6q + \frac{35}{3} q^2 \right), \quad (3)$$

for $q < 1$. For $q > 1$ we set $w(q)$ to zero.

2.2 SPH and SPMHD formulation

It is possible to derive the equations of motion (EOM) in both the hydrodynamical and the magnetohydrodynamical case from a discrete Lagrangian, via the principle of least action, as been presented in Price (2012). This leads to the SPH formulation of the EOM:

$$\frac{d\mathbf{v}_i}{dt} = - \sum_j m_j \left[f_i^{\text{co}} \frac{P_j}{\rho_j^2} \frac{\partial W_{ij}(h_i)}{\partial \mathbf{r}_i} + f_j^{\text{co}} \frac{P_j}{\rho_j^2} \frac{\partial W_{ij}(h_j)}{\partial \mathbf{r}_i} \right], \quad (4)$$

with f_j^{co} given by

$$f_j^{\text{co}} = \left[1 + \frac{h_j}{3\rho_j} \frac{\partial \rho_j}{\partial h_j} \right]^{-1}. \quad (5)$$

The formulation given by equation (4) conserves energy, momentum, and angular momentum per construction. For the case of SPMHD, the EOM take the form

$$\begin{aligned} \frac{d\mathbf{v}_i}{dt} = - \sum_j m_j & \left[f_i^{\text{co}} \frac{P_i + \frac{1}{2\mu_0} B_i^2}{\rho_i^2} \nabla_i W_{ij}(h_i) \right. \\ & + f_j^{\text{co}} \frac{P_j + \frac{1}{2\mu_0} B_j^2}{\rho_j^2} \nabla_i W_{ij}(h_j) \left. \right] \\ & + \frac{1}{\mu_0} \sum_j m_j \left[f_i^{\text{co}} \frac{\mathbf{B}_i [\mathbf{B}_i \cdot \nabla_i W_{ij}(h_i)]}{\rho_i^2} \right. \\ & \left. + f_j^{\text{co}} \frac{\mathbf{B}_j [\mathbf{B}_j \cdot \nabla_i W_{ij}(h_j)]}{\rho_j^2} \right]. \end{aligned} \quad (6)$$

We note that the magnetic field influences the EOM in two ways. At first, the presence of the magnetic field generates a pressure alongside the thermal pressure of the fluid, which scales like \mathbf{B}^2 . The second term is needed to fulfil the $\nabla \cdot \mathbf{B} = 0$ constraint. Further, we note that for the SPMHD formulation, energy and linear momentum are conserved down to machine precision, while angular momentum is violated due to the fact that the second term in equation (6) is anisotropic and therefore not invariant under rotation of the system.

2.3 Cooling, star formation, and supernova seeding

We briefly describe the cooling, star formation, and the SN-seeding approach that is used in a subset of our simulations. We include cooling as described by Katz, Weinberg & Hernquist (1996). In this framework, cooling is mainly driven due to collisional excitation of H^0 and He^+ , and free-free emission (thermal bremsstrahlung). The cooling rates are then calculated via the assumption of collisionless ionization equilibrium and an optically thin gas. We use the

Table 1. Parameters for the multiphase model.

Multiphase model parameters		
Gas consumption time-scale in (Gyr)	t_{MP}	2.1
Mass fraction of massive stars	β_{MP}	0.1
Evaporation parameter	A_0	1000
Effective SN temperature in (K)	T_{SN}	1×10^8
Temperature of cold clouds in (K)	T_{CC}	1000

stochastic star formation approach, presented in Springel & Hernquist (2003), where stars are formed according to the Kennicutt–Schmidt relation (Schmidt 1959; Kennicutt 1989). The adopted values for the star formation model are given in Table 1. Simulations without magnetic fields are referred to as *noB*. Additionally, we perform runs with two different magnetic field models. The first one is set-up with a primordial magnetic field of 10^{-9} G in x -direction in the disc and 10^{-12} G in the CGM, and is referred to as *primB*. The second model does not employ a primordial magnetic field, but follows the magnetic SN seeding presented in Beck et al. (2013), and is referred to as *snB*. Here, a dipole field is seeded in the ISM when a SN explodes, such that it directly couples to the stellar feedback routines. The induction equation is modified with an additional seeding term on the right-hand side:

$$\frac{\partial \mathbf{B}}{\partial t} = \nabla \times (\mathbf{v} \times \mathbf{B}) + \eta \Delta \mathbf{B} + \left(\frac{\partial \mathbf{B}}{\partial t} \right)_{\text{seed}}, \quad (7)$$

with the magnetic resistivity η and the magnetic seeding amplitude per time-step, calculated via

$$\left(\frac{\partial \mathbf{B}}{\partial t} \right)_{\text{seed}} = \sqrt{N_{\text{SN}}^{\text{eff}}} \frac{B_{\text{Inj}}}{\Delta t} \mathbf{e}_B, \quad (8)$$

where $N_{\text{SN}}^{\text{eff}}$ is the effective number of SNe directly given by the Springel & Hernquist (2003) star formation model. The parameter \mathbf{e}_B is a normalization vector and B_{Inj} is the injected magnetic field amplitude given by

$$B_{\text{Inj}} = \sqrt{N_{\text{SN}}^{\text{eff}}} B_{\text{SN}} \left(\frac{r_{\text{SN}}}{r_{\text{SB}}} \right)^2 \left(\frac{r_{\text{SB}}}{r_{\text{Inj}}} \right)^3, \quad (9)$$

with $B_{\text{SN}} = 10^{-5}$ G as the magnetic seed field strength within the SN radius $r_{\text{SN}} = 5$ pc. The bubble radius $r_{\text{SB}} = 25$ pc is the radius where the isotropic expansion of the magnetic field within the shell ends. The bubbles are randomly placed within the injection radius r_{Inj} and mix with the surrounding medium.

3 INITIAL CONDITIONS

Our set-up consists of an isolated disc galaxy, surrounded by a spherical CGM. To set the system up, we use the method described in Hernquist (1993). A more detailed documentation can be found in Springel & White (1999) and Springel, Di Matteo & Hernquist (2005). The model for a spiral disc galaxy consists of a dark matter halo, a bulge, a stellar disc, and a gaseous disc. We prepare initial conditions for three systems with virial masses of 10^{10} , 10^{11} , and $10^{12} M_{\odot}$, representing a dwarf galaxy (DW), a medium-mass galaxy (MM), and a Milky Way-like galaxy (MW), respectively. In Table 2, we present the particle numbers used in our models and list the mass resolution as well as the gravitational softening lengths.

Table 2. Number of particles, mass resolution, and gravitational softening lengths for our three galactic systems.

		Particle numbers (10^6)		
		DW	MM	MW
Gas disc	N_{gd}	0.8	1.0	1.2
Gas halo	N_{gh}	5.0	6.0	7.0
Stellar disc	N_{sd}	3.2	4.0	4.8
Stellar bulge	N_b	1.3	1.6	2.0
Dark matter	N_{dm}	4.6	5.7	6.9
		Mass resolution (M_\odot)		
		DW	MM	MW
Gas particles	m_{gas}	72	510	4800
Star particles	m_{star}	72	510	4800
Dark matter	m_{dm}	1440	10200	96000
		Gravitational softening (pc)		
		DW	MM	MW
Gas particles	ε_{gas}	5	10	20
Star particles	$\varepsilon_{\text{star}}$	5	10	20
Dark matter	ε_{dm}	40	20	10

3.1 Galactic system

The dark matter halo is modelled using the spherical Hernquist (1993) density profile:

$$\rho_{\text{dm}}(r) = \frac{M_{\text{dm}}}{2\pi} \frac{a}{r(r+a)^3}, \quad (10)$$

where M_{dm} is the total mass of the dark matter halo, and a is a scale parameter. For the corresponding Navarro, Frenk & White (1997) profile with an equal inner density profile and a scale length of r_s , the parameter a can be related to the halo concentration c by

$$a = r_s \sqrt{2 [\ln(1+c) - c/(1+c)]}. \quad (11)$$

The density profile of the stellar bulge follows the Hernquist profile:

$$\rho_b(r) = \frac{M_b}{2\pi} \frac{l_b}{r(r+l_b)^3}, \quad (12)$$

where l_b is the scale length of the bulge. Its mass is given by $M_b = m_b M_{200}$, where m_b is the dimensionless bulge mass fraction. The surface densities of the stellar and gaseous discs Σ_* and Σ_{gas} follow an exponential profile:

$$\Sigma_* = \frac{M_*}{2\pi l_d^2} \cdot \exp\left(-\frac{r}{l_d}\right), \quad (13)$$

$$\Sigma_{\text{gas}} = \frac{M_{\text{gas}}}{2\pi l_d^2} \cdot \exp\left(-\frac{r}{l_d}\right), \quad (14)$$

where l_d is the scale length of the disc. The mass of the disc is given by $M_d = (M_* + M_{\text{gas}}) = m_d M_{200}$, with the dimensionless disc mass fraction m_d . We take a fraction f of the disc mass to compose the gaseous disc. The total mass of the dark matter halo is then given by $M_{\text{dm}} = M_{200} - (m_b + m_d) \cdot M_{200}$. Finally, the angular momentum of the system is determined by the spin parameter λ , as described by Mo, Mao & White (1998). The parameters we used for each model are listed in Table 3.

3.2 Circumgalactic medium

Our implementation of the CGM follows that of Moster et al. (2010) and Donnert (2014), but samples the particles from a glass distribution rather than from a random distribution. We assume a radial

Table 3. Adopted parameters for our three galactic systems.

Disc parameters		DW	MM	MW
Total mass ($10^{10} M_\odot$)	M_{200}	1	10	100
Virial radius (kpc)	r_{200}	31	67	145
Halo concentration	c	8	10	12
Spin parameter	λ	0.033	0.033	0.033
Disc mass fraction	m_d	0.041	0.041	0.041
Bulge mass fraction	m_b	0.013	0.013	0.013
Disc spin fraction	j_d	0.041	0.041	0.041
Gas fraction	f	0.2	0.2	0.2
Disc scale length (kpc)	l_d	0.8	1.5	2.1
Disc height	z_0	$0.2 l_d$	$0.2 l_d$	$0.2 l_d$
Bulge size	l_b	$0.2 l_d$	$0.2 l_d$	$0.2 l_d$

symmetric density distribution for the gas medium surrounding the galaxy. For this, we use the radial density profile of the β -model (Cavaliere & Fusco-Femiano 1978), which has also been found by observations (i.e. Croston et al. 2008; Miller & Bregman 2013). The density distribution in the β -model takes the form

$$\rho_{\text{gh}} = \rho_0 \left(1 + \frac{r^2}{r_c^2}\right)^{-\frac{3}{2}\beta}. \quad (15)$$

We follow Mastropietro & Burkert (2008) and set $\beta = 2/3$, which is underpinned by recent observations by Miller & Bregman (2013), who find a value for β close to this value. We choose the central gas density ρ_0 to be between 10^{-27} and $5 \times 10^{-26} \text{ g cm}^{-3}$, motivated by the electron density found through cosmological simulations (Dolag et al. 2015) as well as the observations of Milky Way's hot gaseous halo (Miller & Bregman 2013). The core radius r_c has been chosen between 0.22 and 0.33 kpc, which is again motivated by observations (Miller & Bregman 2013). The value of r_c conforms well with $r_s/40$ where r_s is the scale length of the corresponding NFW halo. The value of $\beta = 2/3$ allows us to calculate the mass distribution of the gaseous halo analytically. By integrating the density profile set by equation (15), the hot gas mass within a radius r is given by

$$M_{\text{gh}}(< r) = 4\pi r_c^3 \rho_0 \left[\frac{r}{r_c} - \arctan\left(\frac{r}{r_c}\right) \right]. \quad (16)$$

As we require the density distribution to be as close as possible to equilibrium, we sample the particle positions of the CGM with a normalized glass distribution. The glass is constructed with the Wendland C4 kernel to be consistent with the disc galaxy simulations. We introduce the variable q as

$$q = \frac{M_{\text{gh}}(< r_{\text{new}})}{M_{\text{gh}}}, \quad (17)$$

which corresponds to the hot gas mass within a radius r_{new} , normalized by the total gas mass of the CGM. To sample the particle distribution, we thus need to solve the equation

$$\frac{4\pi r_c^3 \rho_0}{M_{\text{gh}}} \left[\frac{r}{r_c} - \arctan\left(\frac{r}{r_c}\right) \right] - q = 0. \quad (18)$$

We take a normalized, equally distributed glass distribution and transform its components to spherical coordinates r' , θ , and ϕ . As we can see from equation (16), the mass distribution of the β profile is only a perturbation in the radial coordinate. We determine the value of q that corresponds to r' by solving equation (18) with the Newton–Raphson method.

This leads to a new radial component with a smaller value than r' , in agreement with the density distribution given by equation (15). As this procedure distorts the initial glass sampling, the advantages of using a glass are somewhat weakened. However, the particle noise is kept low enough to justify the procedure (a more rigorous approach will be presented in Arth et al., in preparation). Further, we observe better results compared to other initial configurations (random distribution, cubic, or hcp lattice). The angular coordinates stay unchanged, and we can perform the transformation from spherical coordinates back to Cartesian coordinates with the new radial coordinate. As a result, we get a particle distribution for the CGM that is as close as possible to its dynamical equilibrium. In the last step, the gaseous halo is balanced in the dark matter profile of the galactic disc. The condition for hydrostatic equilibrium between the dark matter halo of the galaxy and the CGM is

$$\frac{1}{\rho_{\text{gh}}} \frac{dP_{\text{gh}}}{dr} = - \frac{G M_{\text{total}}(< r)}{r^2}. \quad (19)$$

This allows us to calculate the temperature profile of the CGM by integrating the equilibrium condition using the ideal equation of state for an atomic gas:

$$T(r) = \frac{\mu m_p}{k_B} \frac{G}{\rho_{\text{gh}}} \int_r^{R_{\text{max}}} \frac{\rho_{\text{gh}}(t)}{t^2} M_{200}(< t) dt, \quad (20)$$

which leads to

$$T(r) = G \frac{\mu m_p}{k_B} \left(1 + \frac{r^2}{r_c^2} \right) [M_{\text{dm}} F_0(r) + 4\pi r_c^3 \rho_0 F_1(r)]. \quad (21)$$

The temperature profile consists of two parts. The first part comes from the dark matter halo and the second part is the influence of the CGM itself. The functions $F_0(r)$ and $F_1(r)$ are given via

$$F_0(r) = \frac{r_c}{a^2 + r_c^2} \left[\frac{\pi}{2} (a^2 - r_c^2) + r_c \frac{a^2 + r_c^2}{a + r} - (a^2 - r_c^2) \arctan \left(\frac{r}{r_c} \right) - r_c a \ln \left(\frac{(a+r)^2}{r^2 + r_c^2} \right) \right], \quad (22)$$

and

$$F_1(r) = \frac{\pi^2}{8r_c} - \frac{\arctan^2(r/r_c)}{2r_c} - \frac{\arctan(r/r_c)}{r}. \quad (23)$$

From an observational point of view, it is useful to calculate a virial temperature for the gaseous halo $T_c = T(r_c)$. It can be calculated as

$$T_c = \frac{2G\mu m_p}{k_B} \left\{ M_{\text{dm}} \frac{r_c^2}{(a^2 + r_c^2)} \cdot \left[\frac{\pi}{4r_c^2} (a^2 - r_c^2) + \frac{a^2 + r_c^2}{a + r_c} - a \ln \left(\frac{(a+r_c)^2}{2r_c^2} \right) \right] + \pi^2 r_c^2 \rho_0 \left(\frac{3\pi}{8} - 1 \right) \right\}. \quad (24)$$

In Table 4, we summarize the values used to construct realistic gaseous haloes for the three galactic system in this study. Finally, we note that the CGM is truncated at R200.

3.3 Combination of the galactic disc with the CGM

Finally, we need to combine the galactic disc with the CGM in a way that keeps the initial conditions as close as possible to equilibrium. Further, we want to avoid an overlap between the particles of the galactic disc and the CGM. Therefore, we implement a procedure to cut out the central part of the CGM and place the disc in the resulting gap. An obvious choice would be to cut out a cylinder,

Table 4. Parameters for the gaseous halo.

General parameters			
Total Mass ($10^{10} M_\odot$)	M_{gh}	DW	MM
Virial temperature (K)	T_{vir}	10^4	10^5
Settings for the β -model			
Exponent	β	$2/3$	
Density in (g cm^{-3})	ρ_0	5×10^{-26}	
Core radius	r_c	$0.22 \cdot r_s$	$0.33 \cdot r_s$

with the radius of the disc and the height of the disc height. This procedure has the advantage that it is very simple. However, this method results in a relatively large gap between the disc and the CGM. Luckily, the density profile of the galactic disc and the CGM are slightly different, and we can use this for selecting the part of the CGM we want to cut out, by introducing a quality condition for the density in the overlap region of galactic disc and CGM. To do so, we bring the SPH data of the galactic disc on a grid using the triangular-shaped cloud (TSC) method. Then, we compare the density of each grid cell to the density of the CGM. To minimize the gap between disc and gaseous halo, we remove the particles of the CGM, if their density is 10 per cent different to that of the grid cell they are related to. The grid we use for this purpose has a spatial resolution of $20^3 = 8000$ cells.

4 RESULTS

We perform three types of simulations with the same initial conditions but with different approaches for the magnetic field, a primordial field, a field seeded by SNe, and, for reference, without a magnetic field. In this section, we present our results for the morphology of the disc, the star formation rate (SFR), the growth rate of the magnetic field, the magnetic field structure, and the interaction between the galactic disc and the CGM. We mainly focus on the Milky Way-like galaxies MW, MW-primB, and MW-snB.

4.1 Morphology of the galactic disc and the magnetic field

We first focus on the most important morphological structures in the simulations, i.e. face-on and edge-on slices of the density and the magnetic field strength for the Milky Way-like models MW-snB and MW-primB. The slices of the face-on view are centred in the mid-plane, the ones for the edge-on view are perpendicular to it. Fig. 1 shows our results for the model MW-snB after $t = 2$ Gyr (first and second columns) and $t = 3$ Gyr (third and fourth columns). The upper left-hand panel shows that the gas in the disc builds up a well-defined spiral structure. The lower left-hand panel indicates that the system evolved to a thin disc that is surrounded by the lower density gas of the CGM. However, because of the density gradient of the underlying β -profile, one can see a brighter blue halo closer to the disc. This density gradient is a quantity that has been introduced by our galactic model itself and is only weakly influenced by the boundary layer between the gas disc and the CGM. In the second panel on the top, we show the face-on view of the absolute magnetic field strength. While the gas density on average decreases monotonically towards the outer parts of the disc, the situation is different for the galactic magnetic field, which is of the order of a few μG in two different regions. This is in good agreement with observations of several spiral galaxies (Beck & Wielebinski 2013; Beck 2015;

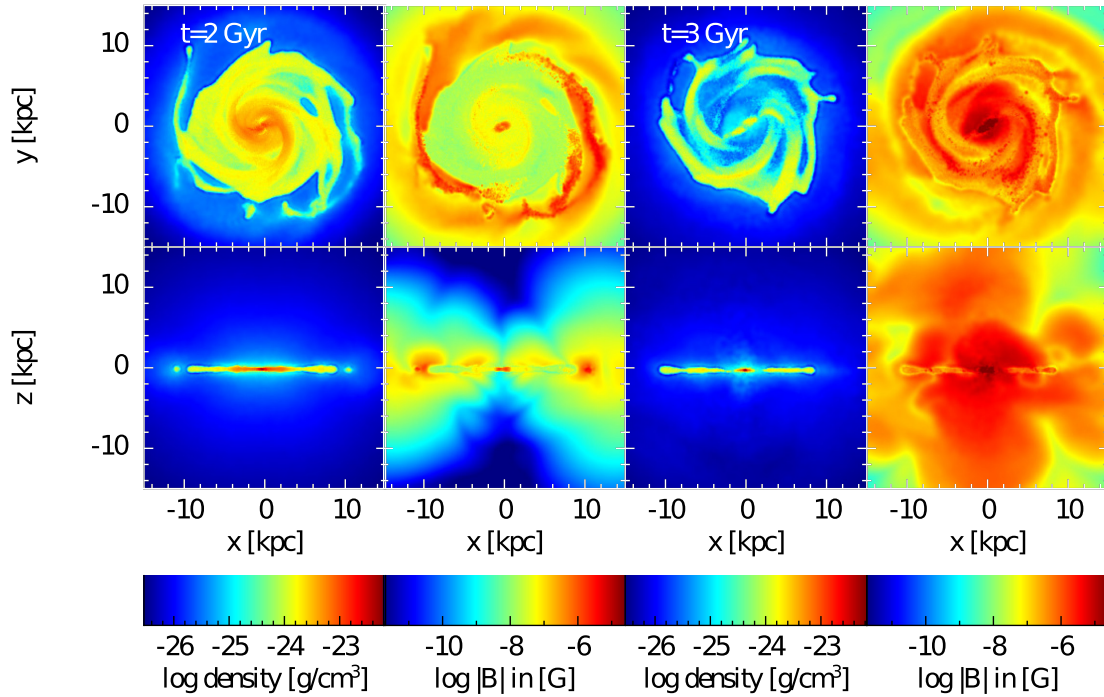


Figure 1. Slice through the gas density and the magnetic field strength for the simulation *MW-snB* for the face-on and edge-on view. The four panels on the left-hand side are at $t = 2$ Gyr, while the four panels on the right-hand side are at $t = 3$ Gyr.

Han 2017). The first region with strong magnetic fields is the very centre of the galactic disc (i.e. the innermost kpc). The second region is a ring-shaped structure further outside in the galactic disc and approximately located at 10 kpc distance from the galactic centre. The former originates from the large SFR in the very centre of the galaxy. A consequence of strong star formation is a large rate of SNe in the same region. In the model MW-snB, this is directly correlated with the amount of magnetic dipoles that are seeded into the surrounding ISM, leading to a strong magnetic field. Furthermore, in this regime the magnetic field is exponentially amplified by the small-scale turbulent motion of the ISM. This small-scale turbulence is mainly driven by the higher SN rate in the centre of the galaxy. We will discuss this in more detail in Section 4.3. In contrast, the amplification process in the outer parts of the disc is most likely not driven by small-scale turbulence. There we observe very high rotation velocities of the gas due to the differential rotation of the disc. This leads to an exponential amplification of the magnetic field through the kinematic motion known as the $\alpha-\omega$ dynamo. This explains the strong magnetic field at the edge of the disc, although the amount of SNe in the ambient medium in the outer parts of the disc is significantly lower compared to the galactic centre. Nevertheless, turbulent motion could also play a crucial role in this regime.

We note that the large magnetic field strengths are correlated with the location of the spiral arms in the gas density, but they do not explicitly follow each other. It seems that the magnetic field strength between or at the edges of the spiral arms in the gas density is higher than in the gaseous spiral arms itself. This behaviour is indicated by observations (see Beck 2015 for a review) and can be explained in galaxies with high density. Strong density waves lead to a compression of the magnetic field at the inner edges of the spiral arms. This can lead to turbulent motion and further amplification of the magnetic field. However, one can hardly see whether the

magnetic field follows the spiral structure of the gas density by only comparing the two top left-hand panels of Fig. 1 at this point in time. The anticorrelation becomes clearer later at $t = 3$. We will evaluate this behaviour in closer detail in Section 4.5. In the bottom row of Fig. 1, we plot the edge-on view of the gas density (first panel) and the magnetic field strength (second panel). Perpendicular to the galactic disc, the magnetic field strength declines much more weakly than the gas density. This is especially true at the edge and is a result of the interaction between the outer parts of the disc with the surrounding CGM. The large magnetic field at the edge leads to a weak magnetization of the nearby CGM. Due to the magnetic pressure, the gas particles near the edge of the disc gain momentum in z -direction, move into the CGM, slow down, magnetize the nearby particles in the CGM, stop, and fall back towards the disc. After $t = 3$ Gyr (third and fourth columns), the face-on view of the gas density shows that the spiral structure is more depleted than at $t = 2$ Gyr. We note that this effect is the strongest in the galactic centre. This can be explained by the higher SFR in the centre of the galaxy. A large fraction of the original gas mass in the centre has been converted into stars that lead to a significant drop in the gas density. In the third panel on the top, we present the face-on view of the magnetic field for $t = 3$ Gyr. To this point in time, the magnetic field strength in the galactic disc has significantly increased and evolved towards a prominent spiral structure. It reaches values of a few $10 \mu\text{G}$ in the magnetic spiral arms to a few $100 \mu\text{G}$ in the galactic centre. The magnetic field in the spiral arms is still in agreement with the observations of magnetic fields in spiral galaxies (e.g. Beck & Wielebinski 2013). The magnetic field in the central region has a maximum value that is around $350 \mu\text{G}$. Although this is a high magnetic field strength, there is observational evidence that the magnetic field in the centre reaches values between $50 \mu\text{G}$ (Crocker et al. 2010) and 4 mG (Yusef-Zadeh et al. 1996).

We further note that at $t = 3$ Gyr, we can clearly observe the magnetic field in the interarm regions to be stronger than in the gaseous spiral arms. We are also able to reproduce the correct field strengths in the interarm regions of a few $10 \mu\text{G}$ that are known from observations (Beck 2007, 2009). Our simulations reach larger field strengths in the interarm regions than in the gaseous spiral arms with the correct field strengths compared to observations. However, the physical reason for this behaviour cannot be clearly determined. There are several possibilities that can lead to stronger magnetic fields in the interarm regions, such as the buoyancy, Parker, or magnetorotational instability (MRI)¹ (Beck 2015). In the centre of the galactic disc, the magnetic field is further amplified by the small-scale turbulent motion of the ISM. This leads to a very huge magnetic pressure in the very innermost kpc of the galactic disc. When the magnetic pressure becomes large enough, it can accelerate particles alongside the z -direction. The strong magnetic field drives the system out of equilibrium, leading to a sharp pressure gradient between the magnetic-dominated disc and the thermal-dominated, hot gaseous halo. As a result, the magnetic field lines break up in z -direction to reduce the sharp pressure gradient at the edge of the disc, and we can observe a biconical outflow of magnetic energy perpendicular to the disc. We note that it has its origin in the very centre of the disc.

Because this biconical magnetic tube is one of the central morphological features, we show it for both magnetic field models (*MW-snB* and *MW-primB*) in Fig. 2 shortly after it sets in at $t = 2.3$ Gyr. The top row of Fig. 2 shows the edge-on gas density (left) and magnetic field (right) for the *MW-snB* run. The bottom row shows the same quantities for the *MW-primB* run. Although magnetic fields are seeded differently in both models, we observe this biconical magnetic tube in both simulations at the exact same time. In the beginning, the magnetic tube rises symmetrically above the disc. It moves forward into the outer parts of the CGM, with a mean velocity of around $400\text{--}500 \text{ km s}^{-1}$. The biconical tube transports a significant amount of magnetic energy into the CGM, leading to its magnetization.

Moreover, this effect leads to morphological features in the gas density of the CGM close to the disc at the onset of the biconical magnetic tube at around $t = 2.3$ Gyr. The nearby CGM shows an X-shaped or H-shaped structure. These structures of the CGM around galaxies are a well-known morphological feature in observations of galaxies with an active galactic nucleus (AGN) in the centre (i.e. Veilleux, Cecil & Bland-Hawthorn 2005). In these observations, it is known as an indicator for a biconical galactic outflow. We note that we do not include such an AGN, but we observe the CGM structures that indicate such an outflow. In our simulations, this outflow would be driven by the magnetic field. Therefore, we discuss the possibility of magnetic driven biconical outflows in more detail in Section 4.4. We note that we observe these X-shaped structures of the CGM around the galaxy only in the first few 100 Myr after the onset of the biconical magnetic tube, and thus we conclude that the magnetic wind should be the strongest shortly after it sets in. We do not find a huge difference in the X-shaped structures around the galaxy between the models *MW-snB* and *MW-primB*.

Nevertheless, we observe slightly higher magnetic field strengths in the biconical tube for the model *MW-snB*. In Fig. 3, we present the exact same properties as in Fig. 1 for the model *MW-primB*. The overall morphological structure is comparable to the model *MW-snB*. We observe a prominent gas disc in the face-on view for $t = 2$ Gyrs as well as a thin gas disc in the edge-on view. Further, we see that the magnetic field is mainly amplified in the galactic centre and in a ring around the centre with a radius of around 10 kpc. As we do not seed magnetic field with SNe, we emphasize that the amplification of the magnetic field in the model *MW-snB* is not caused by a higher magnetic field seeding in the central region due to the higher amount of SNe. In both cases, the SNe are a crucial component for the amplification of the magnetic field in the galactic centre. But the cause for the amplification is the turbulent motion that is driven by SN feedback in the galactic centre leading to an exponential amplification of the magnetic field in the centre. By comparing models *MW-snB* and *MW-primB*, it becomes clear that turbulence induced by SN feedback is the crucial component for the amplification of the magnetic field in the centre. We present more evidence of the small-scale turbulent dynamo in Section 4.3. Further, our results justify the common choice of a primordial seed field, which has often been used by other groups (e.g. Pakmor & Springel 2013; Butsky et al. 2017).

The edge-on view (bottom panels of Fig. 3) shows the same biconical magnetic outflow. Its appearance in the model *MW-primB* leads to the conclusion that this structure in the magnetic field is not driven by the SN seeding. Furthermore, we observe a similar behaviour of the magnetic field in the interarm regions that becomes even clearer for the model *MW-primB* at $t = 3$ Gyr. The model *MW-primB* is also capable of reproducing the observed field strengths in spiral galaxies. To give a more detailed overview of the evolution of the magnetic field, we show a time sequence of the evolution of the magnetic field strength for the model *MW-snB* in Fig. 4. The top panels show the face-on view, and the bottom panels show the edge-on view. The evolution of the magnetic field in the *MW-primB* model is very similar, with only minor differences.

4.2 Star formation rate within the different models

In Fig. 5, we show the SFR for the simulations *MW-snB*, *MW-primB*, and *MW-noB* as a function of time. All simulations were evolved for $t = 4$ Gyr. The SFR at the beginning of the simulation is very similar in all three runs, and peaks shortly after the start of the simulation to a value of around $7 \text{ M}_\odot \text{ yr}^{-1}$. The initial peak can be explained by the non-equilibrium configuration and the large amount of cold gas at the start of the simulation. It is entirely set by the initial conditions, and does not depend on the magnetic field model. After the initial peak, the SFR declines rapidly. In the first 1.5 Gyr, there is no significant difference between the three models, except for a slightly lower SFR for the *MW-primB* run. This small deviation can simply be explained by the difference in the initial magnetic field strength. While the simulations *MW-snB* and *MW-noB* start without any magnetic field, the simulation *MW-primB* starts with a field strength of 10^{-9} G in the disc. This is demonstrated in Fig. 6, which shows the magnetic field strength for the simulations *MW-snB* (red solid line) and *MW-primB* (blue solid line). The mean magnetic field strength of the *MW-primB* run is three orders of magnitude higher in the beginning than in the *MW-snB* run, leading to a higher magnetic pressure, which can result in a lower SFR if gas is pushed out of the star-forming regions of the disc. The SFRs in the simulations *MW-snB* and *MW-noB* are identical in the beginning since the small initial magnetic field

¹At early times, we do not resolve the fastest growing mode of the MRI. For later times, when the magnetic field is saturated the resolution scale of the fastest growing mode is $\sim 20 \text{ pc}$ depending on the exact location across the disc. This length scale is of the same order of magnitude as our force softening and therefore the simulations weakly resolve the MRI at later times.

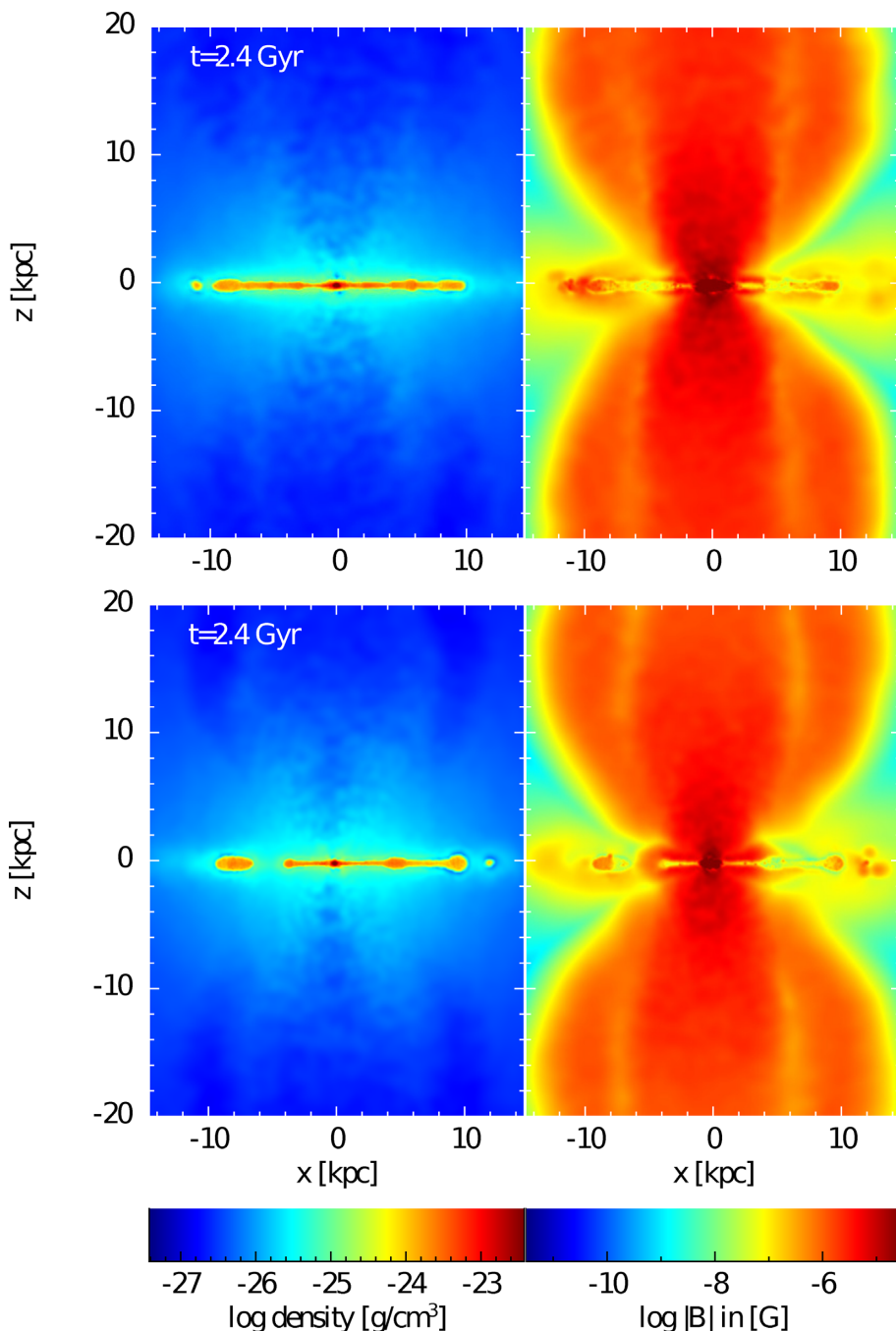


Figure 2. Cross-section slices for the *MW-snB* run (top panels) and the *MW-primB* run (bottom panels) at $t = 2.4$ Gyr. On the left, we show the edge-on view of the gas density and on the right we show the edge-on view of the magnetic field strength. For both models, we observe a strong biconical outflow in the magnetic field strength with an x-shaped structure.

corresponds to the run without a magnetic field and therefore does not change the SFR. After the SFR drops, it remains nearly constant between 1.7 and 2.3 Gyr for all three simulations. Then, the SFR in the simulations with magnetic fields drops by about 50 per cent for the rest of the simulation compared to the simulation without magnetic fields. This indicates that in the *MW-snB* and *MW-primB* runs, a significant amount of the star-forming gas is removed from the disc. This can be explained by the results of Section 4.1, which showed strong magnetized biconical outflows that set in at around $t = 2.3$ Gyr in both runs. This indicates that the SFR is reduced

due to a magnetized outflow of gas from the disc to the CGM. This outflow is driven by the magnetic pressure, i.e. the magnetic field strength within the disc, that rises mainly in the centre due to amplification via small-scale turbulence. This results in a smaller gas reservoir in the disc leading to a lowered SFR. In the star-formation model used in our simulations, all gas above the threshold density forms stars, independent of its temperature and magnetic field strength. Thus, we cannot follow the impact of the magnetic field on the SFR directly, but only its indirect influence, such as outflows that are driven by the contribution of the magnetic pressure

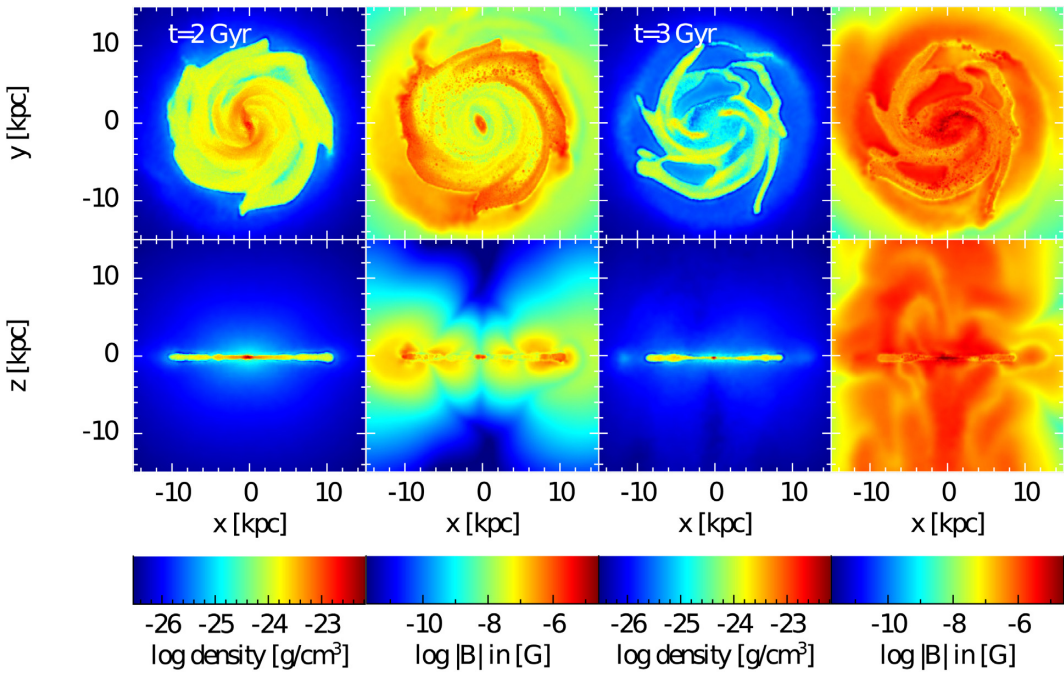


Figure 3. Same as Fig. 1 but for the *MW-primB* simulations. A similar behaviour as in Fig. 1 is observed.

in the ISM. For a more detailed analysis on how the magnetic field influences the galactic SFR, the density threshold in the star formation recipe would have to be changed to a pressure threshold, such that the magnetic pressure $B^2/8\pi$ can be taken into account directly.

4.3 Amplification of the magnetic field

A very important aspect of disc galaxy simulations with SPMHD is to reproduce the observed magnetic field strengths in the disc. There are many observations of magnetic fields in galactic discs (e.g. Hummel 1986; Chyží et al. 2003, 2007; Beck 2007), which show that the field strength in discs ranges from $10 \mu\text{G}$ between the spiral arms up to $50 \mu\text{G}$ within the spiral arms. We present the growth rate of the magnetic field in our three models in Fig. 6. The solid lines represent the magnetic field strength in the galactic disc, for the models with SN seeding (red) and a constant magnetic seed field (blue). The dashed lines represent the magnetic field strength in the CGM. The vertical dashed line marks the point in time when the magnetic pressure becomes dynamically important at around $t = 2.3$ Gyr. At the beginning of the simulation, the magnetic field in the disc roughly grows exponentially in both models, in good agreement with the findings of dynamo theory. In galaxies, there are in general two amplification processes for the magnetic field. The first is the small-scale turbulent dynamo and the second is the mean-field $\alpha-\omega$ dynamo. Both dynamos can lead to either exponential or linear growth of the magnetic field. In the case of the small-scale turbulent dynamo, the amplification of the magnetic field happens due to the turbulent motion in the ISM as long as we can neglect the pressure caused by the magnetic field itself, so that the dynamo operates in the kinetic regime (Pakmor et al. 2017). The magnetic energy rises exponentially until an equilibrium with the kinetic energy is reached. At this point, the magnetic energy can be transported to large scales due to an inverse energy cascade. In

this regime, the small-scale dynamo is only able to follow linear amplification (Federrath 2016). In the case of the $\alpha-\omega$ dynamo, the differential rotation and the α -effect (small-scale vertical motion of the gas particles) in the galactic disc itself can lead to both, exponential or linear growth of the magnetic field. Initially, it is not clear which of those two amplification processes is favoured in our simulations. However, we can deduce the dominant amplification process from the power spectrum of the magnetic field, which is shown for both models in Fig. 7. These power spectra have been obtained with the tool SPHMAPPER (Röttgers & Arth 2018), which carries out an appropriate binning for SPH data on a regular grid using the same kernel that is used in the simulations (Wendland C4). The left-hand panel of Fig. 7 shows the power spectra at five different points in time for the model *MW-snB*. The right-hand panel of Fig. 7 shows the power spectra at the same points in time for the model *MW-primB* field. Both magnetic field models reproduce a relatively smooth distribution of the magnetic power from small scales to large scales. We find strong evidence for a small-scale turbulent dynamo for both magnetic field models. From dynamo theory, we expect a power spectrum $P(k) \propto k^{3/2}$ in the case of a small-scale turbulent dynamo. We can see this behaviour in both power spectra very clearly, especially at the beginning of the simulation, when the equilibrium state between the magnetic and the kinetic energy has not been reached yet. The magnetic field is amplified by turbulent motion on small scales and transported to large scales by an inverse energy cascade, as predicted by dynamo theory. We note that the power spectrum on the large scales is fully consistent with a Kazantsev spectrum (Kazantsev 1968; Kraichnan 1968), known from a small-scale turbulent dynamo (Brandenburg & Subramanian 2005; Tobias, Cattaneo & Boldyrev 2011). This is also consistent with the findings of other simulations of isolated disc galaxies (Rieder & Teyssier 2016, 2017a; Butsky et al. 2017) as well as those of cosmological zoom-in simulations (Pakmor et al. 2017; Rieder & Teyssier 2017b). As this small-scale dynamo is one of the central findings of our study, we provide more evidence based

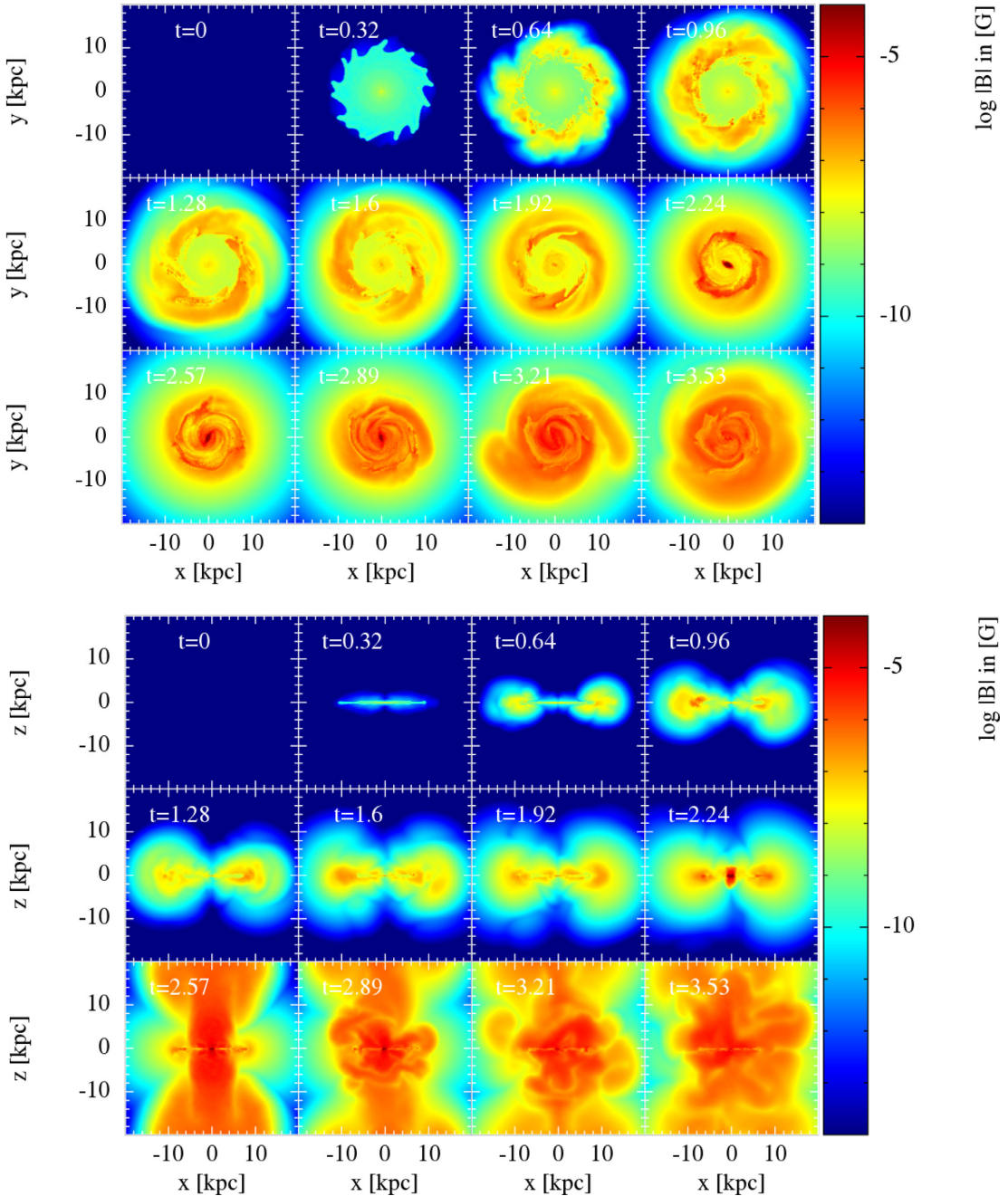


Figure 4. Face-on (top panels) and edge-on (bottom panels) time sequences for the simulation *MW-snB*. The sequence shows the amplification of the magnetic field strength in the galactic disc, as well as the development of the outflow of highly magnetized material perpendicular to the disc.

on the Kazantsev (1968) theory. For this, we calculate the magnetic curvature \mathbf{K} given by Schekochihin et al. (2004):

$$\mathbf{K} = \frac{(\mathbf{B} \cdot \nabla) \mathbf{B}}{|\mathbf{B}^2|}. \quad (25)$$

Using vector identities, we can reformulate equation (25). Thus, we obtain

$$\mathbf{K} = \frac{1}{|\mathbf{B}^2|} \left[\frac{1}{2} \nabla (\mathbf{B} \cdot \mathbf{B}) - \mathbf{B} \times (\nabla \times \mathbf{B}) \right]. \quad (26)$$

The magnetic curvature can be used to distinguish the regime where the magnetic field is amplified by adiabatic compression (i.e. the magnetic field strength stays constant with increasing curvature)

and the regime where a dynamo is acting (Schekochihin et al. 2004; Schober et al. 2015). In this case, an anticorrelation can be found between the magnetic field strength and the curvature with the relation $KB^{0.5} = \text{const}$. We show the median magnetic field strength as a function of curvature in Fig. 8. The red and blue lines correspond to the *MW-snB* and *MW-primB* runs, respectively. The orange line represents the power-law slope indicated by Schekochihin et al. (2004). Further, the black line shows the recent results by Vazza et al. (2018), where the same power-law behaviour is found for a galaxy cluster simulated with the grid code ENZO. We note that the curvature is a very noisy quantity. This has two different origins. The first one is the rapidly changing distributions of both the magnetic field strength, and the curvature in agreement with Schekochihin

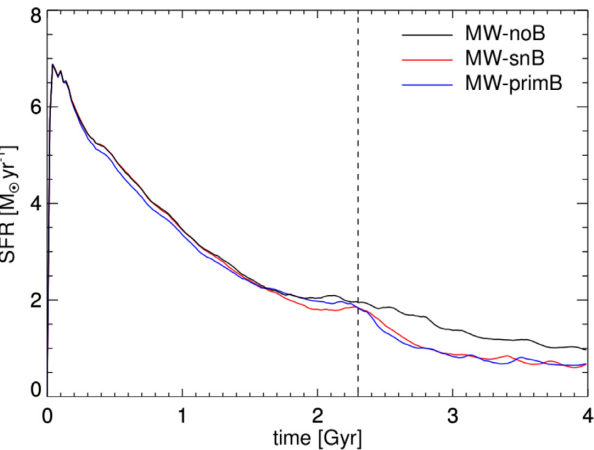


Figure 5. SFRs for the simulations *MW-noB* (black line), *MW-primB* (red line), and *MW-primeB* (blue line). For all three runs, the SFR peaks shortly after the simulation starts due to the non-equilibrium initial condition. At $t = 2.3$ Gyr, the SFR drops for both models that include magnetic fields.

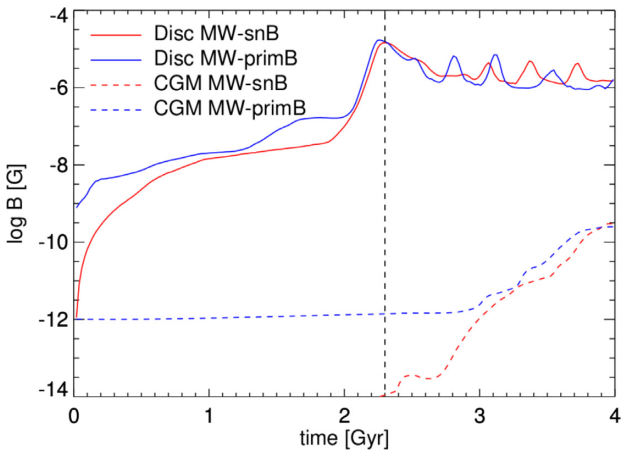


Figure 6. Magnetic field strength for the simulations *MW-snB* (red line) and *MW-primB* (blue line). In the disc, it first grows exponentially and then saturates at $\sim 10^{-6}$ G with oscillations that reach up to a few 10^{-5} G. The dashed lines show the evolution of magnetic field strength in the CGM. The mean magnetic field strength in the CGM is around 10^{-10} G and is still rising when the simulation stops.

et al. (2004). The second one is the low-order gradient estimates that we used for calculating the curvature as a real SPH quantity (e.g. Price 2012). In our simulations, we find the same power-law behaviour as Schekochihin et al. (2004) for the intermediate curvatures between 0.1 and 1, which provides further evidence for a small-scale dynamo in both our magnetic field models. Moreover, in Fig. 8 we indicate the curvature corresponding to the disc scale height with a vertical dashed line. While in a cluster environment the power-law slope of Schekochihin et al. (2004) can be recovered also in the high-curvature regime, this is not the case for our isolated galactic systems. The reason for this may be that the interface between the rotating disc and the halo gives a natural scale on which the field has to be bent. At low curvatures and very strong magnetic fields, we see that the trend of the curvature deviates from the Schekochihin et al. (2004) power law. In this regime, the magnetic field is weakly increasing, while the curvature is staying nearly

constant. This can be identified as a regime where the amplification is driven by adiabatic compression. We find further evidence for this statement by taking Fig. 9 into account, where we present the median magnetic field strength as a function of the gas density for the simulation *MW-snB*. The largest magnetic field strengths coincide with the densest gas in the very centre of the galaxy (in a radius less than 1 kpc). Here, we find that the magnetic field is amplified by adiabatic compression, where we expect a scaling following $B \propto \rho^{2/3}$. This relation can be derived from the flux freezing argument of ideal magnetohydrodynamic (MHD), where we assume that the flux of the magnetic field is conserved. This behaviour is comparable to findings of other simulations such as Marinacci et al. (2015, 2018) and Pakmor et al. (2017). However, the central region is complex due to the fact that all gas particles above 2.5×10^{-25} g cm $^{-3}$ are star forming.

Although we can present strong evidence for a small-scale turbulent dynamo in the power spectra (Fig. 7) and the magnetic curvature (Fig. 8), at later times, the slope of the power spectrum is no longer in agreement with the Kazantsev (1968) power spectrum. This indicates that the amplification process is not dominated by the small-scale dynamo at later times. In this case, we find that our power spectra are similar to an Iroshnikov (1963, 1964) spectrum that is acting in the regime of strong magnetic fields. Examining this behaviour, we believe that the small-scale dynamo is turned off at later times due to the strong dominating magnetic field in the galaxy. This is in agreement with the behaviour we observed in Fig. 6, where we see an exponential growth in the beginning, which becomes linear at later times. The interplay between the Iroshnikov spectrum and the linear growth of the magnetic field at later times leads to the conclusion that the amplification process of the magnetic field in this regime is either driven by the α - ω dynamo instead of the small-scale turbulent dynamo, or switched off completely. The more likely option of these two is the former one that is indicated by the abrupt increase (about two orders of magnitude) of the magnetic field strength at around 2.1 Gyr (see Fig. 6). We can identify this region as a transition region from the small-scale turbulent dynamo to the α - ω dynamo where both processes are acting, but the α - ω dynamo finally takes over once the magnetic fields in the disc are strong enough to effectively suppress turbulence. This point is strengthened by the fact that in Fig. 7 the slope of the power spectra for $t = 2.1$ and $t = 2.2$ starts to deviate from the proposed Kazantsev (1968) spectrum showing first evidence that the small-scale turbulent dynamo is about to shut down. Finally, we note that in the CGM there is nearly no growth of the magnetic field visible. In the *MW-primB* run, there is a small amplification of the magnetic field in the beginning because of the non-zero magnetic field in the CGM in this model and the slight rotation of the CGM. However, the amplification in this case is minimal, and, as expected from dynamo theory, we can see a small exponential growth due to an α - ω dynamo. Because the CGM is in hydrostatic equilibrium due to our initial conditions, there is no amplification of the magnetic field strength over small-scale turbulence.

Although there is no relevant magnetic field in the CGM in the first 2.3 Gyr of the simulation, after around 2.3 Gyr we see a jump in the magnetic field strength in the CGM of several orders of magnitude in both models. There is no observable difference in the behaviour of the magnetic field strength in the CGM between both our models. This underpins the fact that the observed magnetic field in our simulations depends mainly on the dynamical structure of the galaxy and is not dominated by the seeding of the magnetic field.

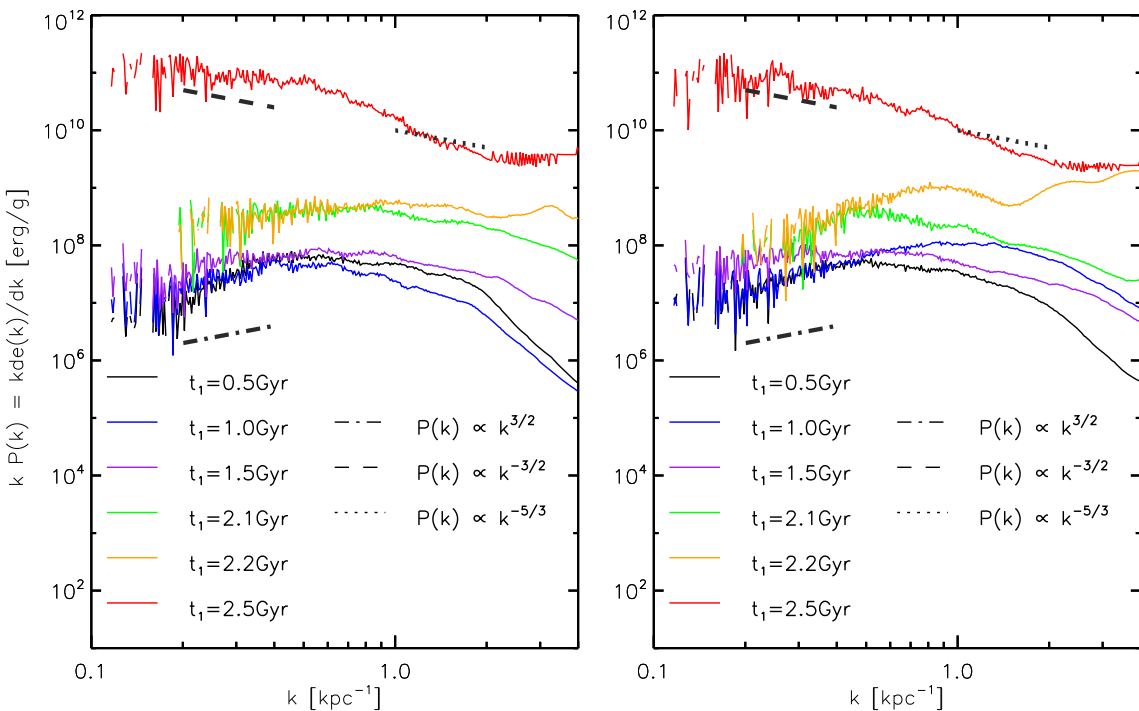


Figure 7. Magnetic power spectra for the simulations *MW-snB* (left-hand panel) and *MW-primB* (right-hand panel). Both models result in very similar power spectra, independent of the seeding model. The magnetic field is amplified by turbulent motion on small scales, which is transported to large scales through an inverse energy cascade. This Kazanetzov (1968) spectrum is an indicator for a small-scale turbulent dynamo, resulting in an increase of the power $P(k) \propto k^{3/2}$ on large scales. The small-scale dynamo stops at later times due to the large magnetic field resulting in an Froshnikov (1963) spectrum with $P(k) \propto k^{-3/2}$.

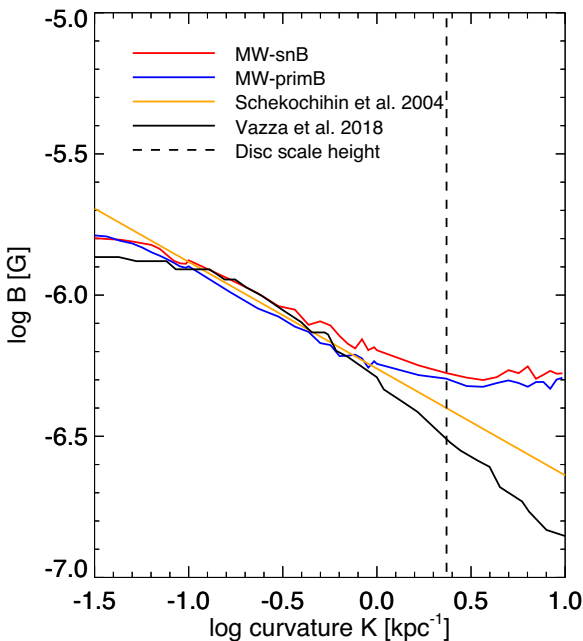


Figure 8. Median of the magnetic field strength as a function of the curvature of the magnetic field lines for $t = 2$ Gyr. The red line represents the *MW-snB* run and the blue line the *MW-primB* run. The field strength and curvature are anticorrelated with a power-law slope of 0.5, as the field lines are harder to bend in the presence of stronger magnetic fields. The slope indicates that the amplification is driven by small-scale turbulence in agreement with the results by Schekochihin et al. (2004; orange line). The black line shows the recent result of MHD-simulations of galaxy clusters by Vazza et al. (2018).

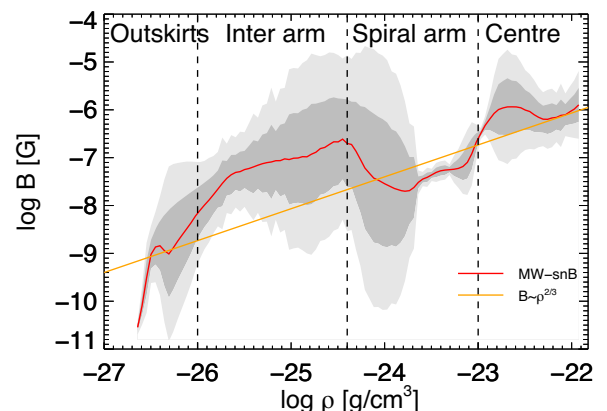


Figure 9. Median magnetic field strength for the model *MW-snB* (red) alongside with its 1σ (dark grey shaded region) and 2σ (light grey shaded region) errors. The orange line shows the relation that is known from the flux freezing argument of MHD, indicating amplification by adiabatic compression that can be found in several recent simulations (Marinacci et al. 2015, 2018; Pakmor et al. 2017). The highest magnetic field strengths correlate with the highest gas densities. In the centre, the gas density is driven by both adiabatic compression and small-scale turbulence. In the spiral arms, the magnetic field is lower compared to the interarm region and is amplified by adiabatic compression. The magnetic field strength in the interarm regions is amplified by small-scale turbulence and not adiabatic compression. In the outskirts of the galaxy, the amplification is not driven by adiabatic compression.

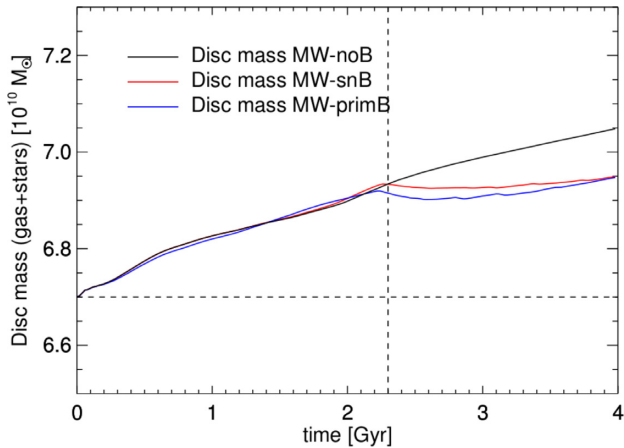


Figure 10. Total mass of the disc for the simulations *MW-noB* (black), *MW-snB* (red), and *MW-primB* (blue). While the disc is accreting a large amount of gas in *MW-noB*, the net growth of the disc is suppressed in *MW-snB* and *MW-primB*, after the magnetic outflow sets in at 2.3 Gyr.

4.4 Halo accretion and magnetic driven outflows

A new and very important aspect of our simulations is the inclusion of the CGM, unlike in previous simulations of isolated disc galaxies (e.g. Kotarba et al. 2011; Butsky et al. 2017). This allows us to observe the interaction of an isolated disc galaxy with its CGM in an idealized environment without any perturbations. In Section 4.3, we have shown that the CGM gets strongly magnetized because of outflows that transport a lot of the magnetic power, which is amplified in the galactic disc via the small-scale turbulent dynamo and the mean field $\alpha-\omega$ dynamo, to the outer parts of the CGM. We observe a prominent tube with a radius of approximately 2 kpc near the disc, which opens up to 5 kpc in its outer parts with a magnetic field strength between 10^{-7} and 10^{-6} G. It reaches the outer parts of the CGM with a total length of around 40 kpc. This magnetic tube transports gas out of the disc in positive and negative z -direction at nearly the same rate, with a speed of a few 100 km s^{-1} . Some of the gas particles are close to reaching the galactic escape velocity. The gas is moving outwards along the magnetized tube and falls back to the disc from outside the tube, such that there is an active exchange of the disc's gas with the hot gas of the CGM. Further, we note that after the onset of the magnetic tube we see heavily magnetized, low-density bubbles rising from the galactic disc to the CGM reaching a height of a few kpc above the disc, which is in agreement with the findings of Pakmor & Springel (2013). In addition to the gas that is initially located in the disc, moves to the CGM, and falls back, there is also a cooling flow of hot gas from the CGM on to the disc. To demonstrate this, we show the evolution of the total mass of the baryonic disc for our three models in Fig. 10. While cold gas is turned into stars, the total disc mass increases with time, as the disc is fuelled by cooling gas from the hot halo. Interestingly, the cooling rate ($1 \text{ M}_\odot \text{ yr}^{-1}$) is roughly of the same order as the SFR ($\sim 3 \text{ M}_\odot \text{ yr}^{-1}$), indicating that the disc can compensate the loss of gas mass due to star formation by accreting hot gas from the CGM. Because of the immense gas reservoir, the SFR in the disc is thus stabilized, and eventually reaches an equilibrium. After the magnetic outflow sets in, the total disc mass stays roughly constant, while in the simulation without magnetic fields the disc still grows by accreting gas from the CGM at a constant rate. Thus, for both magnetic field models the strong magnetic driven wind with about one solar mass

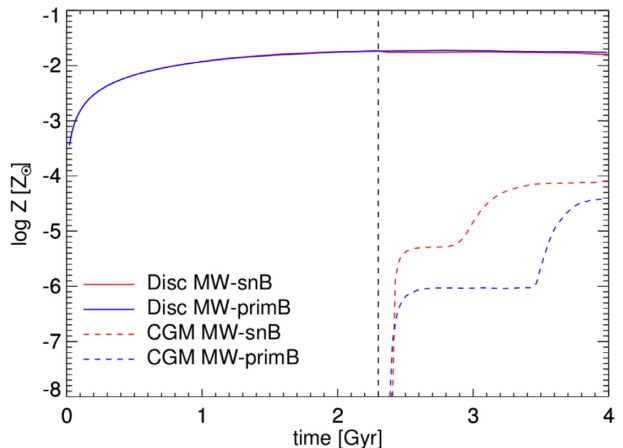


Figure 11. Time evolution of metals in the disc (solid lines) and the CGM (dashed lines) for *MW-snB* (red) and *MW-primB* (blue). The black vertical dashed line indicates the onset of the outflow driven by magnetic fields, leading to a net magnetization of the CGM in both models that is normally believed to be obtained by the wind feedback induced by SNe.

per year, compensates the incoming cooling flow. This equilibrium between inflow and outflow results in a constant disc mass, although within the disc, cold gas is still converted into stars. We note that the outflow velocities and mean magnetic field strengths in the biconal outflow we observe are fairly similar to the properties observed in the ‘Fermi bubbles’. In Carretti et al. (2013), a magnetic field strength between 6 and 12 μG is observed for the two lobes that is comparable to the field strengths between 1 and 30 μG we find in the biconal outflow in our simulations. Further, in our simulations we find that these biconal structures propagate with a velocity between 400 and 500 km s^{-1} into the CGM, while kinematic modelling of the Fermi bubbles leads to outflow velocities between 1000 and 1300 km s^{-1} as presented by Bordoloi et al. (2017).

Along with the outflowing gas, the metals that are returned to the disc by SN feedback are transported to the CGM. We show this behaviour for the models *MW-snB* (red) and *MW-primB* (blue) in Fig. 11. The solid lines represent the metals in the disc and the dashed lines the metals in the CGM. We observe metal enrichment in the CGM due to the magnetic outflow, which is normally believed to be caused only by SN-driven winds from either late SN-driven winds in massive galaxies (e.g. Aguirre et al. 2001; Adelberger et al. 2003; Shen et al. 2012) or outflows from dwarf galaxies at higher redshift (e.g. Dekel & Silk 1986; Mac Low & Ferrara 1999; Furlanetto & Loeb 2003). Another mechanism for the metal enrichment of the CGM is proposed by Scannapieco & Oh (2004) due to quasar-driven winds. Gnedin (1998) points out the importance of protogalaxy mergers at high redshift to enrich the surrounding medium with metals. Finally, we note that we could not observe any metal enrichment towards the CGM in the simulation *MW-noB*.

4.5 Magnetic field structure

The general morphological properties of the magnetic field have been discussed in Section 4.1. Here, we present a more detailed study on the galactic magnetic field in our simulations. For this, we show a more detailed comparison between the structure of the gas density and the magnetic field strength in polar coordinates for the *MW-snB* and *MW-primB* runs in Figs 12 and 13, respectively. The left-hand side panels show the gas density and the right-hand side

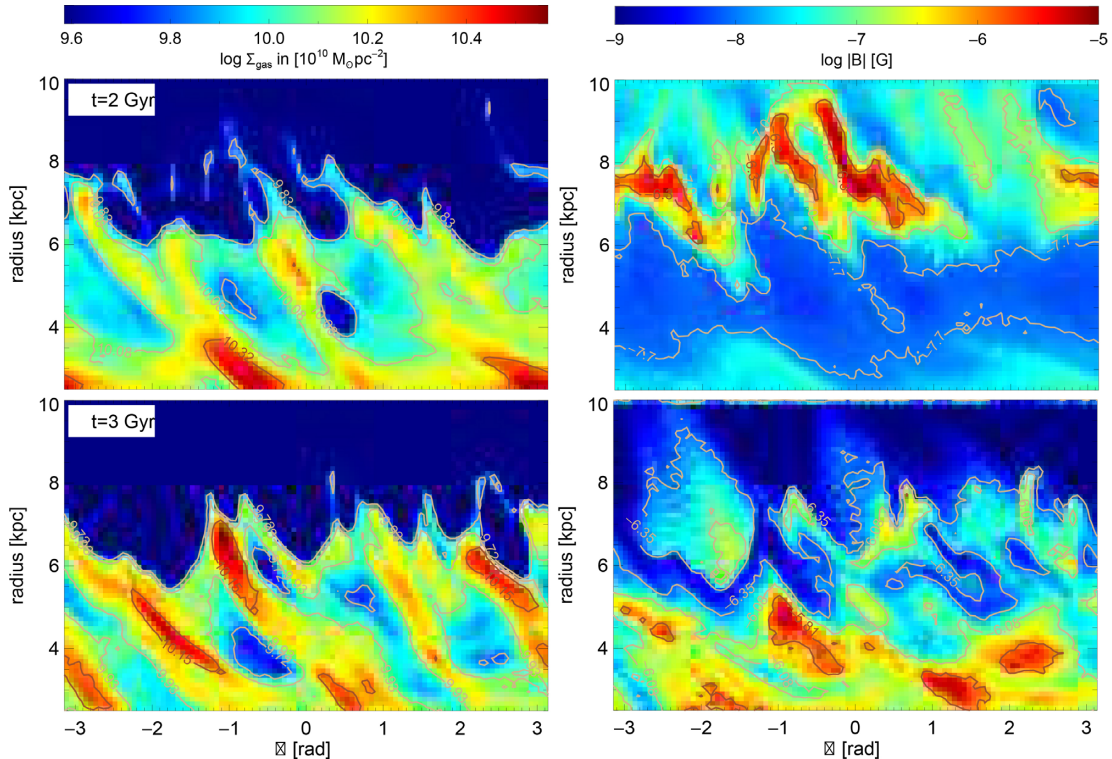


Figure 12. Surface density of the gas (left-hand-side panels) and magnetic field strength (right-hand-side panels) in cylindrical coordinates for the *MW-snB* run at 2 Gyr (top panels) and 3 Gyr (bottom panels), respectively. The spiral structures in the magnetic field and the gas surface density are correlated in the centre at $t = 3$ Gyr, while they are not at $t = 2$ Gyr. In the outer regions of the disc, the magnetic field and the gas density are anticorrelated at $t = 3$ Gyr.

panels show the magnetic field strength, while the panels on the top give the results after $t = 2$ Gyr and the panels on the bottom give the results after $t = 3$ Gyr. Plotting these quantities in polar coordinates allows us to directly compare our results to observations of spiral galaxies, e.g. by Bittner et al. (2017). These plots have been obtained using a 2D grid of the size 100×66 , with a pixel corresponding to a specific r and φ . For each pixel, we calculate the gas density and the magnetic field using the TSC method for calculating densities on a regular grid. The plots then show a slice for a fixed r for one circulation over the whole galaxy. This allows us to determine the positions of the more prominent areas in the structure of a spiral galaxy. The panel on the top left of Fig. 12 nicely shows four density peaks, corresponding to at least four spiral arms in the *MW-snB* simulation, as expected for a Milky Way analogue. Comparing our results for the gas density to the magnetic field strength, we find that they are not strongly correlated. Moreover, early in the simulation, we observe that the magnetic field is stronger in the outer parts of the galactic disc, compared to the centre. This behaviour changes at later times (bottom panels), when the magnetic field is stronger in the centre and shows a spiral structure. The magnetic field strength is highest between the spiral arms of the gas disc, which is most obvious at late times, when the gas of the disc is already depleted due to star formation and outflows. While Beck & Wielebinski (2013) have noted this effect before, they have not found this behaviour in gas-rich galaxies. Although we can give an explanation for the connection between the gas density and the magnetic field strength, we note that our implementation of MHD follows mainly ideal MHD with a small magnetic diffusion term. In the limit of small magnetic fields, this leads to a direct correlation between high densities and high magnetic fields. Thus, at early times

the strongest magnetic fields are located in the high-density areas due to adiabatic collapse and increased turbulent amplification due to the higher SN rate in this regime. At later times, the non-linear term we include in the induction equation makes it possible to trigger diffusive processes that can transport the magnetic field energy from high-density regions to low-density regions. The interarm regions have lower densities and higher temperatures compared to the spiral arms. This leads to a stronger turbulence in these regions than in the spiral arms itself. Once the magnetic field energy is transported via diffusive processes from the spiral arms to the interarm regions, it can be amplified easily via small-scale turbulence on Myr time-scales. This can lead to a dominating magnetic field in the interarm regions. Moreover, we quantify that in Fig. 9 where we can see an overall decrease of the magnetic field strength in the spiral arms compared to the interarm regions of the galaxy.

We now focus on the detailed structure of the magnetic field and the comparison of the differences in the structure for both presented magnetic field models. We present two ways to evaluate this. The first one is based on the evaluation of the quantity ζ_1 given by

$$\zeta_1 = \frac{|\mathbf{B} - \mathbf{B}_{\text{sm}}|}{|\mathbf{B}_{\text{sm}}|}, \quad (27)$$

where \mathbf{B} is the magnetic field and \mathbf{B}_{sm} is the magnetic field smoothed by a Gaussian kernel. As our simulations were performed with an SPH code, ζ_1 cannot be directly computed, but the particle properties first need to be transformed to a regular grid. To achieve this, an obvious choice would be the TSC method that was used to obtain Figs 12 and 13. However, the TSC method is based on a triangular kernel and thus not accurate enough to resolve the detailed structure of the magnetic field in an SPMHD simulation.

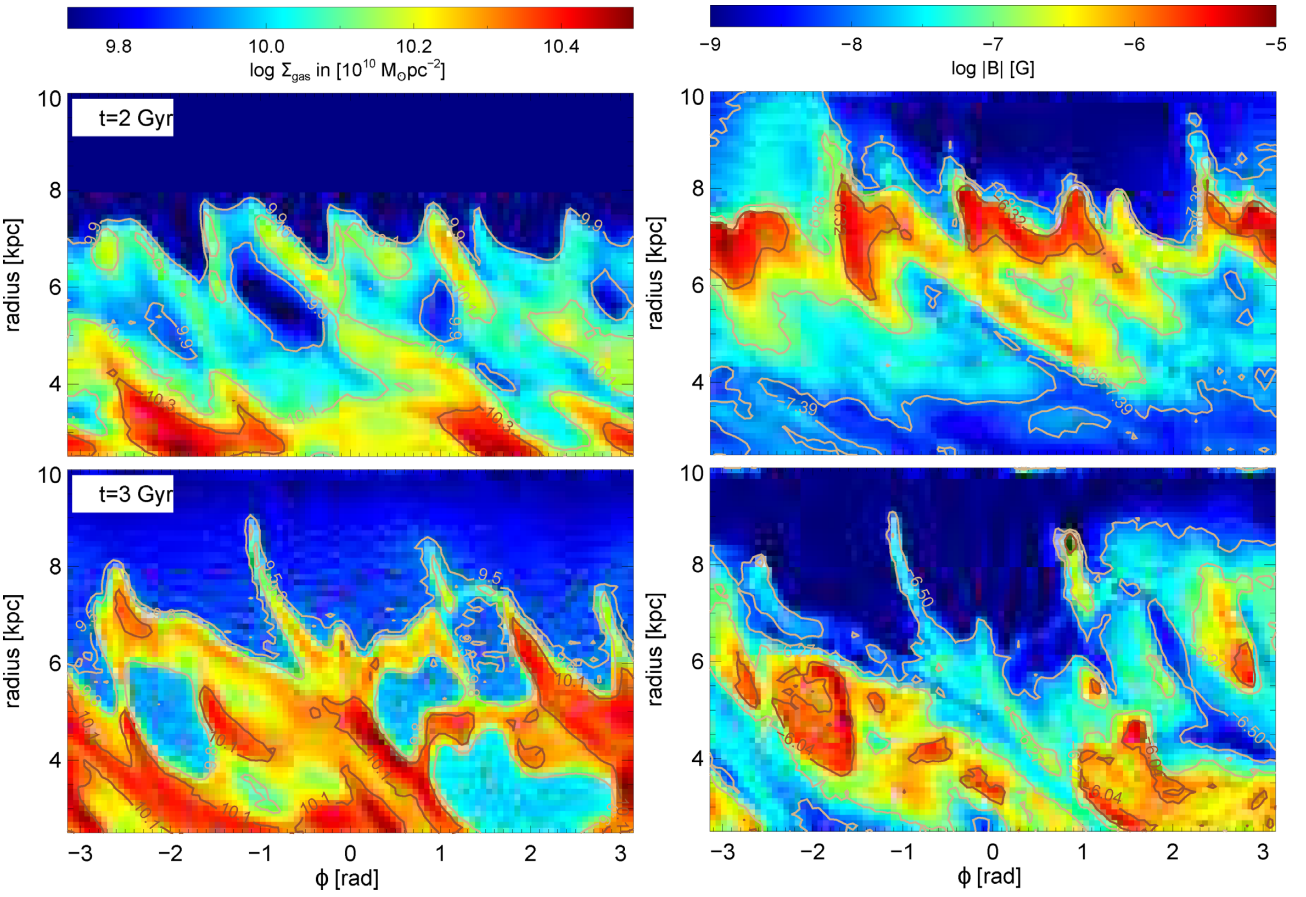


Figure 13. Same as Fig. 12, but for the simulation *MW-primB*.

Therefore, we work out a proper SPH-binning for which we use a 2D grid with a very high resolution of 1024×1024 grid points. For each element, we then calculate the magnetic field with the Wendland C4 Kernel using 200 neighbouring particles. In this way, we use exactly the same configuration to bin the data as for our underlying SPH formalism. The data binning has been performed using the code SPHMAPPER presented by Röttgers & Arth (2018). The property ζ_1 describes the deviation of the magnetic field in our simulations from the smoothed magnetic field. This method, called unsharp masking, is very common in image editing and allows us to achieve a stronger contrast in the magnetic field, making it easier to find detailed structure lines. A high value of ζ_1 indicates a large difference between the smoothed magnetic field and the original magnetic field, indicating a highly turbulent magnetic field. A small value of ζ_1 shows little deviation between the smoothed magnetic field and the original one, indicating a region of highly correlated magnetic field lines.

The upper left-hand panel of Fig. 14 shows ζ_1 for the *MW-snB* simulation at $t = 2.0$ Gyr, shortly before the outflow sets in. It demonstrates that there are detailed structures in the magnetic field beyond the spiral arms. Furthermore, the turbulent structures are mostly located in the centre of the galactic plane. This nicely illustrates that the magnetic field is amplified via a small-scale dynamo, as we argued in Section 4.3. On the small scales, i.e. in the galactic centre, the turbulent character of the magnetic field dominates. The upper right-hand panel of Fig. 14 shows ζ_1 for the *MW-primB* simulation. Also here, we observe the spiral structure of the magnetic field, but the disc is more dominated by turbulence

than in the *MW-snB* run. The bottom panels of Fig. 14 show ζ_1 at $t = 3$ Gyr, demonstrating that the structure of the magnetic field is not diminished by the magnetic outflow that sets in around $t = 2.3$ Gyr. The quantity ζ_1 evaluates the total magnetic field, ignoring the spatial behaviour of each magnetic field component. We therefore present a second method to evaluate the structure of the magnetic field and introduce the variable ζ_2 :

$$\zeta_2 = \sqrt{\left(\frac{B_x - B_{x/sm}}{B_{x/sm}}\right)^2 + \left(\frac{B_y - B_{y/sm}}{B_{y/sm}}\right)^2 + \left(\frac{B_z - B_{z/sm}}{B_{z/sm}}\right)^2}. \quad (28)$$

Compared to ζ_1 , it takes into account the structure of the magnetic field in each spatial direction, and prevents an overestimation due to the strong magnetized outflows in z -direction. The resulting maps are presented in Fig. 15. While the ζ_1 maps clearly show the underlying magnetic structure of the disc in the x - y plane, the ζ_2 maps are far smoother, though we can see the structures we already saw in Fig. 14. Finally, we note that the magnetic field becomes much more turbulent when the magnetic outflow sets in.

4.6 Different halo masses

So far, we focused on the simulations *MW-noB*, *MW-snB*, and *MW-primB*, as these systems were constrained by X-ray observations. Here, we investigate the effects in haloes of lower mass, i.e. $M_h = 10^{11} M_\odot$ (*MM-noB*, *MM-snB*, *MM-primB*) and $M_h = 10^{10} M_\odot$ (*DW-noB*, *DW-snB*, *DW-primB*). While the MM

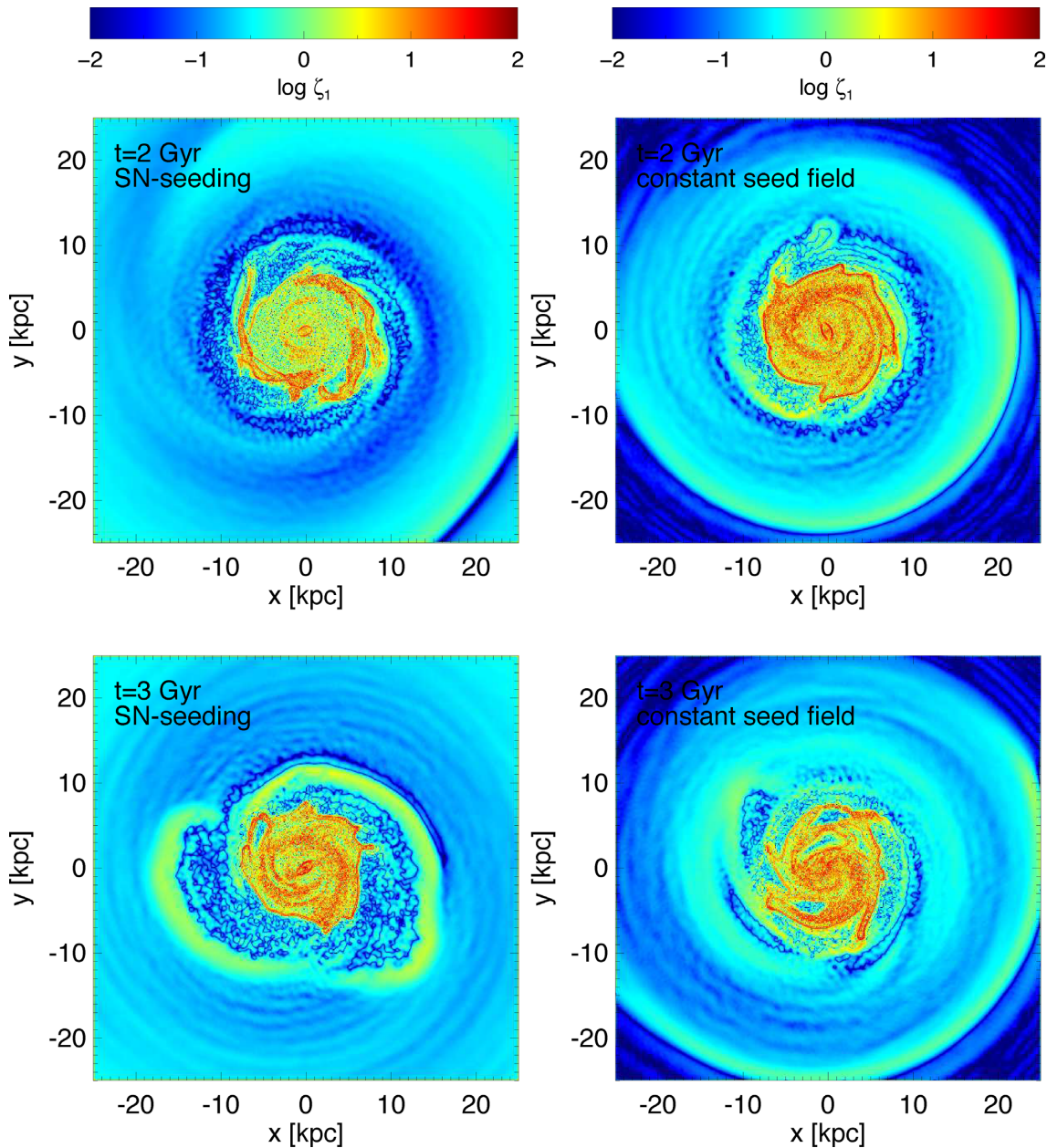


Figure 14. Structure of the magnetic field for the *MW-snB* run (left-hand-side panels) and the *MW-primB* run (right-hand-side panels) at $t = 2$ Gyr (upper panels) and $t = 3$ Gyr (bottom panels), respectively. The colour bar indicates the normalized relative deviation of the magnetic field from a smoothed magnetic field (unsharp masking, see equation 27). The red indicates that turbulence is dominating, while the blue indicates high order in the magnetic field.

systems show a similar behaviour as the MW systems for the amplification of the magnetic field and the observed morphological features, the point in time where the biconical magnetic tube sets in is delayed to $t = 3.0$ Gyr. This is a consequence of the magnetic field amplification being driven by small-scale turbulence induced by feedback, mainly in the galactic centre. In the lower mass galaxies, the efficiency of the feedback is lower, resulting in a slower amplification of the magnetic field. Moreover, the lower rotational velocity in a halo with $M_h = 10^{11} M_\odot$ delays the amplification process further. As a consequence, the magnetic pressure rises at a lower rate compared to the MW systems, such that the magnetic pressure needed to expel gas from the centre towards the CGM is reached at a later point in time. The total magnetic field strength rises to similar values as for the MW models, but the peak values of

the magnetic field is slightly lower, reaching values between 10^{-7} and 10^{-5} G. While the magnetic field properties of the MM simulations are similar to the MW simulations, i.e. a small-scale turbulent dynamo drives the amplification of the magnetic field resulting in an outflow of gas, we notice a considerable difference in the evolution of the SFR. Moreover, we can observe the same transition from the small-scale turbulent dynamo to the $\alpha-\omega$ dynamo as in the MW models including a transition regime where both dynamos seem to act before the small-scale turbulent dynamo is ultimately switched off and the $\alpha-\omega$ dynamo takes over. For the system with the lowest mass of $M_h = 10^{10} M_\odot$ (DW), we only find minor changes for the simulations with magnetic fields compared to the reference simulation without magnetic fields. For this halo mass scale, the magnetic

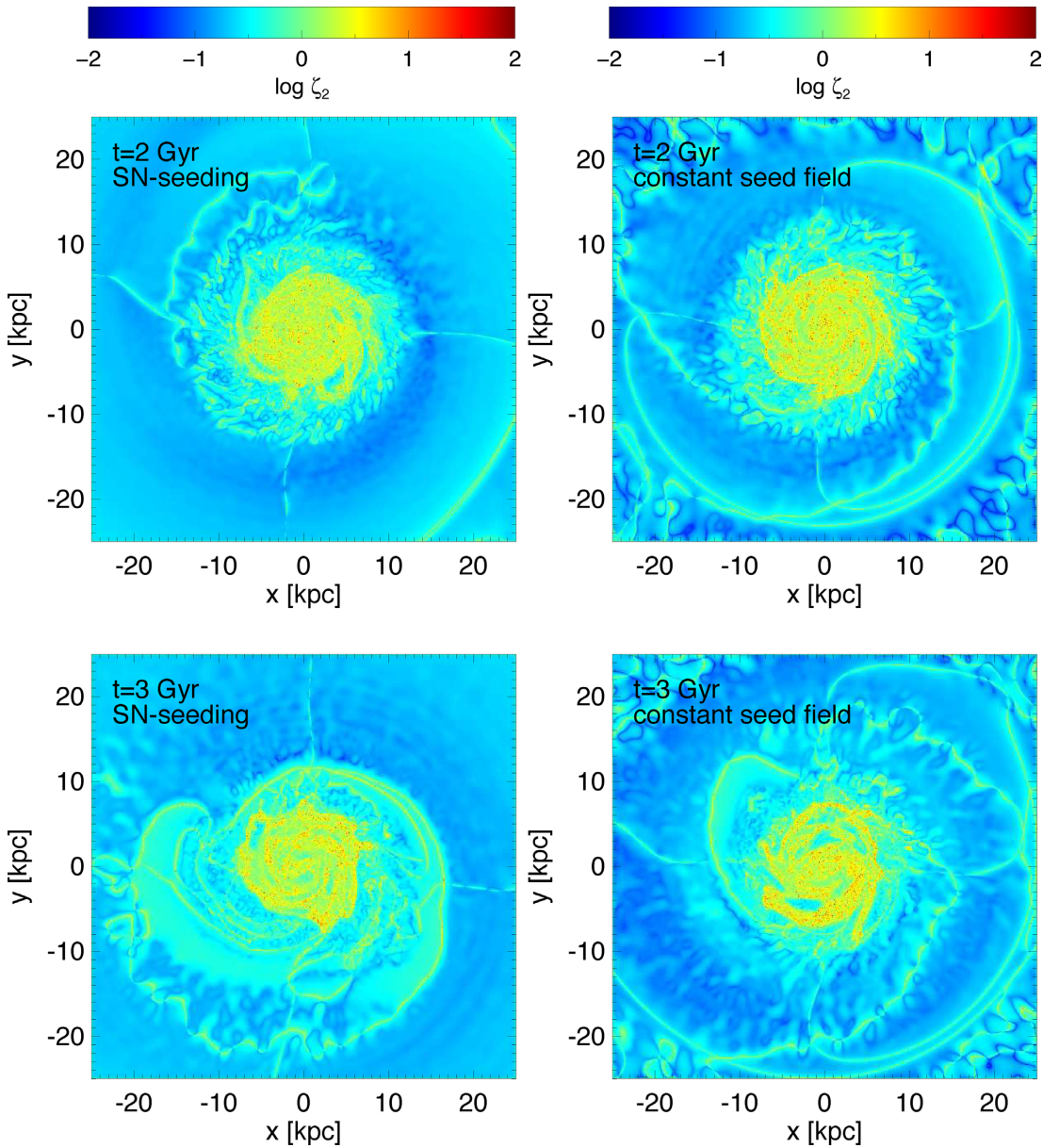


Figure 15. Same as Fig. 14, but each spatial magnetic field direction is normalized to the smoothed magnetic field in that certain direction (see equation 28).

field is dynamically unimportant, as the amplification of the magnetic field is very slow. Since the SFR in these systems is very low, the effects of the SN feedback are minor, resulting in no significant small-scale turbulence that could amplify the magnetic field in the centre. Moreover, the amplification of the magnetic field cannot be supported via the $\alpha-\omega$ dynamo either because the gas orbits with a peak velocity of 50 km s^{-1} . Lastly, the magnetic field can also not be amplified by adiabatic compression of the gas because the potential wells are too shallow to trigger the formation of high-density regions, which would result in an amplification of the magnetic field. Consequently, there are no outflows for the DW simulations. We conclude that outflows are only present when the magnetic field becomes dynamically important. This is the case for the MW and MM haloes because the amplification of the magnetic field is strong enough to reach a magnetic pressure that is higher than the thermal pressure. Therefore, we also do not find transition regions from one

dynamo process to the other. Overall, these lower mass systems seem to be mostly inactive regarding dynamo amplification.

4.7 Divergence cleaning

Every numerical simulation that includes magnetic fields has to deal with the $\nabla \cdot \mathbf{B} = 0$ constraint. We need to prove that our simulations are not contaminated by magnetic monopoles. For this, we present the relative magnetic divergence $h \cdot \nabla \mathbf{B} / |\mathbf{B}|$, where h is the smoothing length, for the *MW-snB* run in Fig. 16, and for *MW-primB* in Fig. 17. The panels on the left-hand side and right-hand side show the result before ($t = 2.0$ Gyr) and after ($t = 3.0$ Gyr) the magnetic outflow sets in. The more turbulent structure after the outflow sets in leads to an increase of the divergence of the magnetic field due to the sharper gradients. The maximum value of the relative divergence error of ~ 1 is reached where turbulence is dominating,

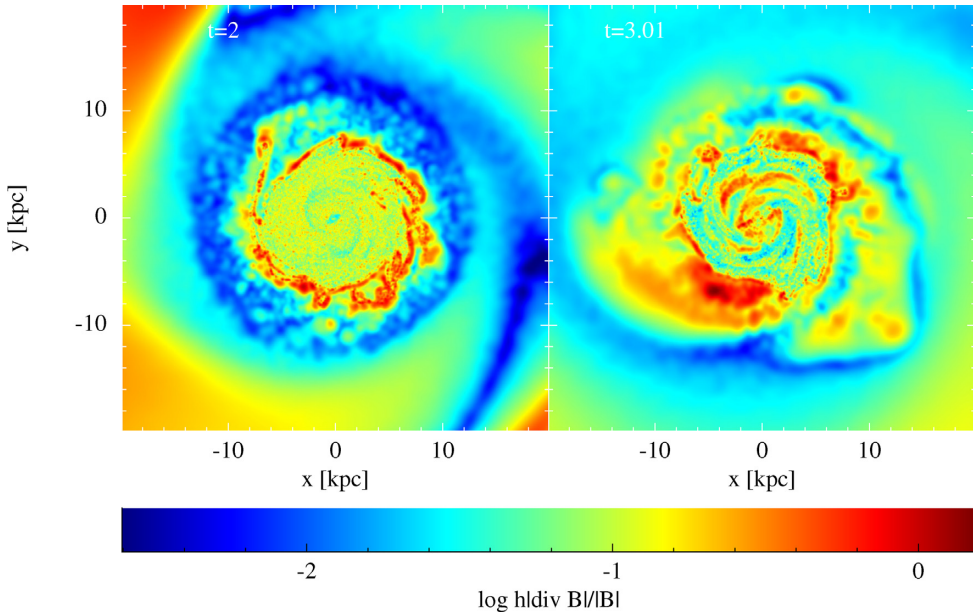


Figure 16. Relative divergence errors for the simulation *MW-snB* at $t = 2$ Gyr (left-hand-side panel) and $t = 3$ Gyr (right-hand-side panel). Typical values are between 1 and 10 per cent.

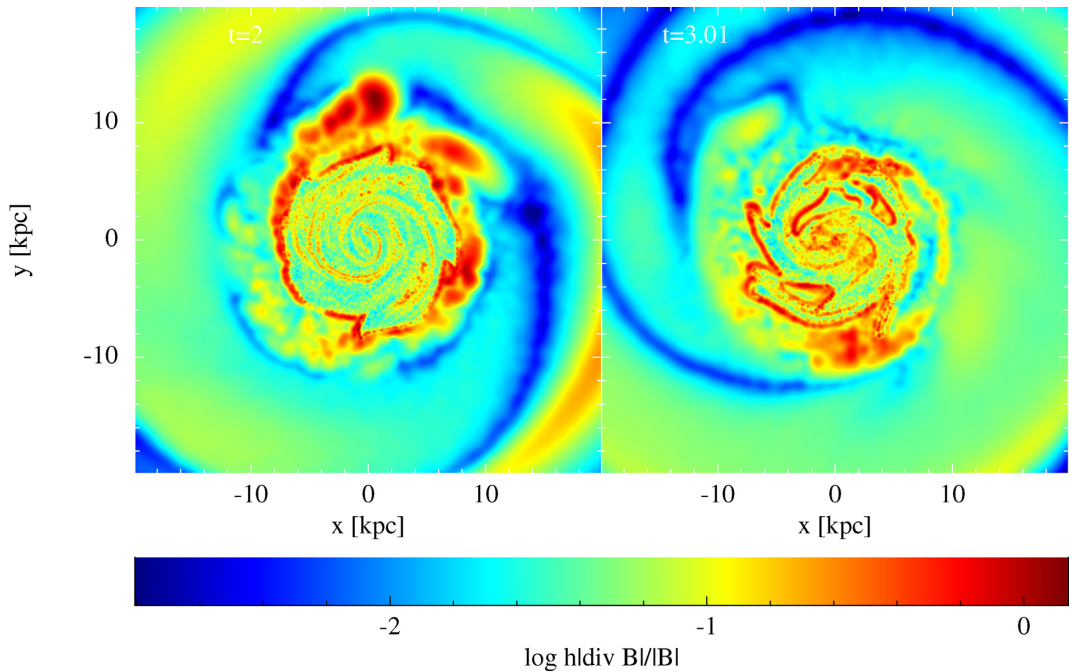


Figure 17. Same as Fig. 16 but for the simulation *MW-primB*.

such as in the galactic centre, and at the edges of the spiral arms. This is comparable to the error in other simulations (e.g. Pakmor & Springel 2013).² However, the typical value of $h \cdot \nabla \mathbf{B} / |\mathbf{B}|$ is below 0.1, which is very good for an SPMHD code. We note that there are

²We note that the magnetic energy density is about a factor of 100 below the kinetic energy density within one resolution element of the simulation in its very centre.

methods in grid codes such as RAMSES, which can reduce the relative divergence error to machine precision. Although these cleaning methods perform very well in test studies, they have the disadvantage of being computationally very expensive. However, Pakmor & Springel (2013) used a cleaning scheme (Powell et al. 1999) similar to ours and find that it is sufficient on a moving mesh. Compared to a regular grid, it is significantly more complicated to control the divergence error on a moving mesh because of the irregularity of the Voronoi-grid, which is similar for an SPH particle distribution.

Although our SPMHD formulation includes higher order hyperbolic cleaning schemes (Dedner et al. 2002; Dolag & Stasyszyn 2009), the findings of Pakmor & Springel (2013) show that it is sufficient to use a lower order cleaning scheme for the type of systems we are simulating. To save computational power, we follow this approach and use a lower order cleaning scheme. We can further observe that the higher values of the relative divergence error appear around the spiral arms, as this is where the magnetic field has strong gradients. This behaviour improves with higher resolution because the gradients become better resolved. Lastly, we note that the divergence is smaller in the case of the SN seeding since magnetic dipoles are inserted into the ISM. By construction, this leads to a lower divergence, as the dipole structure is forced to appear with the SN explosions, resulting in a smoother distribution of the magnetic field.

5 CONCLUSIONS

We present a modified model for isolated disc galaxies including a realistic CGM. Using this model, we simulate a set of galaxies with different halo masses ranging from $10^{10} M_{\odot}$ over $10^{11} M_{\odot}$ to $10^{12} M_{\odot}$ and study the general properties (such as the morphological structure and the SFR) of these systems. We focus on the MW system, and present a detailed study of the morphological structure of the gas density as well as the magnetic field. We observe a mean magnetic field strength of a few μG in the galactic disc, which is in good agreement with observations. In the galactic centre, we find higher field strengths up to a few $100 \mu\text{G}$. In the spiral arms, the magnetic field strength is about an order of magnitude lower compared to the galactic centre. We find that the structure of the magnetic field strength does not follow exactly the spiral arms in the gas density, but is strongest between two neighbouring spiral arms. This result differs from those reported by other groups (Pakmor & Springel 2013; Butsky et al. 2017). The reason for that is that we include a magnetic diffusion term in our simulations, which makes it possible to follow the magnetic field evolution in the non-linear regime. Furthermore, this effect is in agreement with many observations (see Beck 2015 for and references therein). The amplification of the magnetic field in our simulations is mainly driven by small-scale turbulence. We show clear evidence for this in the magnetic power spectra (Fig. 7), in agreement with simulations by other groups (Pakmor & Springel 2013; Rieder & Teyssier 2016; Butsky et al. 2017).

Moreover, we find further evidence for a small-scale dynamo by examining the curvature of the magnetic field lines, which can be used to distinguish between amplification by adiabatic compression and by a small-scale dynamo (Fig. 8). Our simulations indicate that at later times the slope of the magnetic power spectra turns around. This shows that the galaxies are entering a new regime that is dominated by strong magnetic fields instead of small-scale turbulence. Thus, the dominating amplification process in this regime is either driven by the $\alpha-\omega$ dynamo or completely saturated and thus switched off. In the simulations with $M_h = 10^{12} M_{\odot}$ and $M_h = 10^{11} M_{\odot}$, we find galactic outflows that are driven by the magnetic field. In this regime, the magnetic pressure is several orders of magnitude higher than the thermal pressure. In our simulations with $M_h = 10^{10} M_{\odot}$ this is not the case, so that we do not observe a dominating magnetic outflow in haloes below $M_h = 10^{11} M_{\odot}$. A more detailed study of the interaction between galactic disc and CGM shows that a certain amount of magnetic energy is released in the outer regions of the CGM having its origin in the centre of the galac-

tic disc. Studying the turbulence in the magnetic field, we find that the highly magnetized outflows are mainly driven by the turbulent magnetic field in the centre of the galactic disc. The structural analysis of the magnetic field indicates that it follows a complex structure besides the obvious spiral patterns and does not necessarily follow the spiral structure of the gas density because of magnetic diffusion. Finally, we summarize the three most important findings of this study:

(i) The amplification of the magnetic field strength can be divided in different regimes. In the very centre, we find that the magnetic field is amplified by adiabatic compression. However, the main amplification process is driven by small-scale turbulence until the magnetic field in the disc is strong enough so that the dynamo saturates. We provide evidence for this Kazantsev (1968) dynamo in the magnetic power spectra as well as the anticorrelation of the magnetic field strength and the curvature of the magnetic field lines for a small-scale dynamo (e.g. Schekochihin et al. 2004; Vazza et al. 2018). Finally, at later times when strong magnetic fields are present the small-scale turbulent dynamo is switched off, and the system is dominated by the $\alpha-\omega$ dynamo.

(ii) Galaxies in which the magnetic pressure dominates the thermal pressure show magnetic-driven outflows that can lead to a significant mass-loss of the baryonic disc. The outflows appear as low-density bubbles reaching a several 100 km s^{-1} before they mix with the CGM and fall back to the disc.

(iii) Diffusive terms in the induction equation can transport the magnetic field energy from the spiral arms to the interarm regions. In the interarm regions, the density is lower but the temperature is higher that leads to more turbulence and therefore stronger amplification due to the small-scale turbulent dynamo. Thus, we can see an anticorrelation between the spiral structure of the gas disc and the spiral structure within the magnetic field strength that can be seen in observations (Beck 2015).

Future work will need to focus on detailed resolution studies to determine the spatial and the mass resolution that is needed to actually resolve the small-scale turbulent dynamo, which may be crucial in the framework of cosmological zoom-in simulations of MW galaxies. Furthermore, none of the current models for star formation in hydrodynamical simulations include the pressure given by the magnetic field directly. Only indirect effects on the SFR can be captured by the current simulations. In future studies, the magnetic pressure may be directly included using pressure-based star formation models.

ACKNOWLEDGEMENTS

We thank the anonymous referee for his/her comments that helped to improve this work. We thank Eirini Batziou, Andreas Burkert, Julien Devriendt, Timo Halbesma, Stefan Heigl, Thorsten Naab, Rüdiger Pakmor, Rhea Silvia Remus, Felix Schulze, Romain Teyssier, and Simon White for useful discussions and their insights on magnetic fields and galaxies. We thank Franco Vazza for his insights on the magnetic curvature. The authors gratefully acknowledge the computing time granted by the John von Neumann Institute for Computing (NIC) provided on the supercomputer JURECA at Jülich Supercomputing Centre (JSC) under the project number hmz07 and the computing time provided by the Leibniz Rechenzentrum (LRZ) of the Bayrische Akademie der Wissenschaften on SuperMuc in Garching with the project number pe86re. UPS and BPM are funded by the Deutsche

Forschungsgemeinschaft (DFG, German Research Foundation) with the project number MO 2979/1-1. KD acknowledges support by the DFG Cluster of Excellence ‘Origin and Structure of the Universe’.

REFERENCES

- Adelberger K. L., Steidel C. C., Shapley A. E., Pettini M., 2003, *ApJ*, 584, 45
- Aguirre A., Hernquist L., Schaye J., Katz N., Weinberg D. H., Gardner J., 2001, *ApJ*, 561, 521
- Beck R., 2007, *A&A*, 470, 539
- Beck R., 2009, *Astrophys. Space Sci. Trans.*, 5, 43
- Beck R., 2015, *A&AR*, 24, 4
- Beck R., Wielebinski R., 2013, *Magnetic Fields in Galaxies*. Springer, Dordrecht, 641
- Beck M. C., Beck A. M., Beck R., Dolag K., Strong A. W., Nielaba P., 2016a, *J. Cosmol. Astropart. Phys.*, 5, 056
- Beck A. M., Hanasz M., Lesch H., Remus R.-S., Stasyszyn F. A., 2013, *MNRAS*, 429, L60
- Beck A. M. et al., 2016b, *MNRAS*, 455, 2110
- Biermann L., 1950, *Z. Nat.forsch. A*, 5, 65
- Biermann L., Schlüter A., 1951, *Phys. Rev.*, 82, 863
- Bittner A., Gadotti D. A., Elmegreen B. G., Athanassoula E., Elmegreen D. M., Bosma A., Muñoz-Mateos J.-C., 2017, *MNRAS*, 471, 1070
- Bordoloi R. et al., 2017, *ApJ*, 834, 191
- Brandenburg A., Subramanian K., 2005, *Phys. Rep.*, 417, 1
- Brown J. C., Havercorn M., Gaensler B. M., Taylor A. R., Bizunok N. S., McClure-Griffiths N. M., Dickey J. M., Green A. J., 2007, *ApJ*, 663, 258
- Bryan G. L., Norman M. L., 1997, in Clarke D. A., West M. J., eds, ASP Conf. Ser. Vol. 123, Computational Astrophysics; 12th Kingston Meeting on Theoretical Astrophysics. Astron. Soc. Pac., San Francisco. p. 363
- Bryan G. L. et al., 2014, *ApJS*, 211, 19
- Butsky I., Zrake J., Kim J. -h., Yang H. -I., Abel T., 2017, *ApJ*, 843, 113
- Carretti E. et al., 2013, *Nature*, 493, 66
- Cavaliere A., Fusco-Femiano R., 1978, *A&A*, 70, 677
- Chyžík K. T., Knipk J., Bomans D. J., Klein U., Beck R., Soida M., Urbanik M., 2003, *A&A*, 405, 513
- Chyžík K. T., Bomans D. J., Krause M., Beck R., Soida M., Urbanik M., 2007, *A&A*, 462, 933
- Crocker R. M., Jones D. I., Melia F., Ott J., Protheroe R. J., 2010, *Nature*, 463, 65
- Croston J. H. et al., 2008, *A&A*, 487, 431
- Dalla Vecchia C., Schaye J., 2012, *MNRAS*, 426, 140
- Dedner A., Kemm F., Kröner D., Munz C.-D., Schnitzer T., Wesenberg M., 2002, *J. Comput. Phys.*, 175, 645
- Dehnen W., Aly H., 2012, *MNRAS*, 425, 1068
- Dekel A., Silk J., 1986, *ApJ*, 303, 39
- Dolag K., Stasyszyn F., 2009, *MNRAS*, 398, 1678
- Dolag K., Gaensler B. M., Beck A. M., Beck M. C., 2015, *MNRAS*, 451, 4277
- Donnert J. M. F., 2014, *MNRAS*, 438, 1971
- Dubois Y., Teyssier R., 2010, *A&A*, 523, A72
- Federrath C., 2016, *MNRAS*, 457, 375
- Furlanetto S. R., Loeb A., 2003, *ApJ*, 588, 18
- Geng A., Kotarba H., Bürzle F., Dolag K., Stasyszyn F., Beck A., Nielaba P., 2012a, *MNRAS*, 419, 3571
- Geng A., Beck A. M., Dolag K., Bürzle F., Beck M. C., Kotarba H., Nielaba P., 2012b, *MNRAS*, 426, 3160
- Gnedin N. Y., 1998, *MNRAS*, 294, 407
- Hanasz M., Otmianowska-Mazur K., Kowal G., Lesch H., 2009, *A&A*, 498, 335
- Han J. L., 2017, *ARA&A*, 55, 111
- Han J. L., Manchester R. N., van Straten W., Demorest P., 2018, *ApJS*, 234, 11
- Hernquist L., 1993, *ApJS*, 86, 389
- Hogan C. J., 1983, *Phys. Rev. Lett.*, 51, 1488
- Hummel E., 1986, *A&A*, 160, L4
- Iroshnikov P. S., 1963, *Astron. Zh.*, 40, 742
- Iroshnikov P. S., 1964, *Sov. Astron.*, 7, 566
- Katz N., Weinberg D. H., Hernquist L., 1996, *ApJS*, 105, 19
- Kazantsev A. P., 1968, *Sov. J. Exp. Theor. Phys.*, 26, 1031
- Kennicutt R. C., Jr., 1989, *ApJ*, 344, 685
- Kotarba H., Lesch H., Dolag K., Naab T., Johansson P. H., Stasyszyn F. A., 2009, *MNRAS*, 397, 733
- Kotarba H., Karl S. J., Naab T., Johansson P. H., Dolag K., Lesch H., Stasyszyn F. A., 2010, *ApJ*, 716, 1438
- Kotarba H., Lesch H., Dolag K., Naab T., Johansson P. H., Donnert J., Stasyszyn F. A., 2011, *MNRAS*, 415, 3189
- Kraichnan R. H., 1968, *Phys. Fluids*, 11, 945
- Kulsrud R. M., Anderson S. W., 1992, *ApJ*, 396, 606
- Kulsrud R. M., Cen R., Ostriker J. P., Ryu D., 1997, *ApJ*, 480, 481
- Lesch H., Hanasz M., 2003, *A&A*, 401, 809
- Mac Low M. -M., Ferrara A., 1999, *ApJ*, 513, 142
- Malyshkin L., Kulsrud R. M., 2002, *ApJ*, 571, 619
- Marinacci F., Vogelsberger M., Mocz P., Pakmor R., 2015, *MNRAS*, 453, 3999
- Marinacci F. et al., 2018, *MNRAS*, 480, 5113
- Mastropietro C., Burkert A., 2008, *MNRAS*, 389, 967
- Miller M. J., Bregman J. N., 2013, *ApJ*, 770, 118
- Mishustin I. N., Ruzmaikin A. A., 1972, *Sov. J. Exp. Theor. Phys.*, 34, 233
- Moster B. P., Macciò A. V., Somerville R. S., Johansson P. H., Naab T., 2010, *MNRAS*, 403, 1009
- Mo H. J., Mao S., White S. D. M., 1998, *MNRAS*, 295, 319
- Navarro J. F., Frenk C. S., White S. D. M., 1997, *ApJ*, 490, 493
- O’Shea B. W., Bryan G., Bordner J., Norman M. L., Abel T., Harkness R., Kritsuk A., 2004, preprint ([arXiv:astro-ph/0402171](https://arxiv.org/abs/astro-ph/0402171))
- Pakmor R., Springel V., 2013, *MNRAS*, 432, 176
- Pakmor R. et al., 2017, *MNRAS*, 469, 3185
- Plummer H. C., 1911, *MNRAS*, 71, 460
- Powell K. G., Roe P. L., Linde T. J., Gombosi T. I., De Zeeuw D. L., 1999, *J. Comput. Phys.*, 154, 284
- Price D. J., 2012, *J. Comput. Phys.*, 231, 759
- Rieder M., Teyssier R., 2016, *MNRAS*, 457, 1722
- Rieder M., Teyssier R., 2017a, *MNRAS*, 471, 2674
- Rieder M., Teyssier R., 2017b, *MNRAS*, 472, 4368
- Robishaw T., Quataert E., Heiles C., 2008, *ApJ*, 680, 981
- Röttgers B., Arth A., 2018, preprint ([arXiv:1803.03652](https://arxiv.org/abs/1803.03652))
- Ruzmaikin A., Sokolov D., Shukurov A., 1988b, *Nature*, 336, 341
- Ruzmaikin A. A., Turchaninov V. I., Zeldovich I. B., Sokoloff D. D., 1979, *Ap&SS*, 66, 369
- Ruzmaikin A. A., Sokolov D. D., Shukurov A. M., 1988a, *Astrophysics and Space Science Library Vol. 133, Magnetic fields of galaxies*. Springer, Berlin
- Scannapieco E., Oh S. P., 2004, *ApJ*, 608, 62
- Schekochihin A. A., Cowley S. C., Hammett G. W., Maron J. L., McWilliams J. C., 2002, *New J. Phys.*, 4, 84
- Schekochihin A. A., Cowley S. C., Taylor S. F., Maron J. L., McWilliams J. C., 2004, *ApJ*, 612, 276
- Schleicher D. R. G., Banerjee R., Sur S., Arshakian T. G., Klessen R. S., Beck R., Spaans M., 2010, *A&A*, 522, A115
- Schmidt M., 1959, *ApJ*, 129, 243
- Schober J., Schleicher D. R. G., Federrath C., Bovino S., Klessen R. S., 2015, *Phys. Rev. E*, 92, 023010
- Shen S., Madau P., Aguirre A., Guedes J., Mayer L., Wadsley J., 2012, *ApJ*, 760, 50
- Springel V., 2005, *MNRAS*, 364, 1105
- Springel V., 2010, *MNRAS*, 401, 791
- Springel V., Hernquist L., 2003, *MNRAS*, 339, 289
- Springel V., White S. D. M., 1999, *MNRAS*, 307, 162
- Springel V., Di Matteo T., Hernquist L., 2005, *MNRAS*, 361, 776
- Teyssier R., 2002, *A&A*, 385, 337

- Tobias S. M., Cattaneo F., Boldyrev S., 2011, The Nature of Turbulence, Cambridge University Press, Cambridge, p. 351
- Vazza F., Brunetti G., Brüggen M., Bonafede A., 2018, *MNRAS*, 474, 1672
- Veilleux S., Cecil G., Bland-Hawthorn J., 2005, *ARA&A*, 43, 769
- Wang P., Abel T., 2009, *ApJ*, 696, 96
- Wetzstein M., Nelson A. F., Naab T., Burkert A., 2009, *ApJS*, 184, 298
- Widrow L. M., 2002, *Rev. Mod. Phys.*, 74, 775
- Yusef-Zadeh F., Roberts D. A., Goss W. M., Frail D. A., Green A. J., 1996, *ApJ*, 466, L25

- Zeldovich I. B., Ruzmaikin A. A., Sokolov D. D., 1983, Magnetic fields in astrophysics, The Fluid Mechanics of Astrophysics and Geophysics. Vol. 3, Gordon and Breach Science Publishers, New York

This paper has been typeset from a $\text{\TeX}/\text{\LaTeX}$ file prepared by the author.